nature immunology

Article

https://doi.org/10.1038/s41590-025-02285-6

Spatial and functional diversity of innate lymphoid cells in the human female genital tract may contribute to antiviral responses to HIV

Received: 21 November 2024

Accepted: 22 August 2025

Alexandra Werner[1,2,3], **Laura Moreno de Lara**[4,8], **Aleah Holmes**[1,2,3,8], **Siddharth Parthasarathy**[1], **Genna E. Moldovan**[3,5], **Anna Borchers**[4], **Francisco J. Carrillo-Salinas**[4], **Jared M. Fortier**[3,5], **Vidya Iyer**[6,7], **Alison Vogell**[6], **Rebecca Jameson**[5], **Jacquelyn Stephens**[5] **& Marta Rodriguez-Garcia**[1,2,3] ✉

Innate lymphoid cells (ILCs) are tissue-resident lymphocytes specialized in cytokine secretion that lack antigen-specific receptors. The contribution of ILCs to antiviral mucosal immunity in humans, particularly in the female genital tract (FGT), remains unexplored. Here we resolved human FGT ILC diversity by spectral flow cytometry and CITE-seq, spatial location within genital anatomical regions using ChipCytometry, and determined homeostatic function and antiviral responses. We uncovered spatial and functional specializations of genital ILC subsets under homeostasis, with compartmentalized age-related and pregnancy-related changes. CD161 expression differentially discriminated ILC subsets preloaded with cytokines at steady state. We identified a unique NKp44$^+$CCR6$^+$ ILC3 subset in the endometrium that actively degranulated at homeostasis and was located in lymphoid aggregates surrounded by B cells and T cells. By contrast, ILC1s were found scattered, enriched in the ectocervix and located close to the epithelium. Following in vitro HIV stimulation, genital ILCs displayed rapid subset-specific antiviral responses. These findings reveal distinct tissue and subset-specific features of FGT ILCs and their capacity to immediately respond to viral stimuli, providing a foundation for future studies to determine the potential role of ILCs in mucosal immune protection in the FGT.

Women acquire human immunodeficiency virus (HIV) primarily through sexual transmission[1]. However, under non-inflammatory conditions, HIV transmission rates per sexual act are low (0.08%) but as high as 2.65% in the context of sexually transmitted infections[2]. Protective mechanisms in the FGT include intact epithelial barriers, mucus, secretions and innate immune cells[3–8]. Despite this knowledge, we still lack an understanding of the initial events of infection and how to enhance FGT mucosal protection. This is in part because initial mucosal host–pathogen interactions that determine whether infection is prevented or established happen very quickly (within minutes) and cannot be captured in vivo. To develop effective preventative methods, it is imperative to dissect the early events of mucosal HIV acquisition and how the different innate immune cells respond to HIV in the female genital mucosa, one of the main portals of entry for HIV.

ILCs are tissue-resident lymphocytes that lack antigen-specific receptors and specialize in cytokine secretion. Helper ILCs are grouped

---

A full list of affiliations appears at the end of the paper. ✉e-mail: Marta.rodriguez-garcia@wayne.edu

into three main populations (ILC1s, ILC2s and ILC3s) that functionally resemble T_H1, T_H2 and T_H17 CD4$^+$ helper T cells[9]. ILC1s produce interferon-γ (IFNγ); ILC2s secrete IL-5, IL-13 and IL-9; and ILC3s produce IL-22 and IL-17 in response to stimuli[9]. Murine ILCs contribute to barrier integrity and mucosal protection against infection[10], but ILCs in human mucosal surfaces and their contribution to mucosal protection remain largely uncharacterized[11–13].

Tissue-specific adaptations, lack of lineage markers and overall rare presence make human ILC characterization difficult and highlight the need to define human ILC subsets in their tissue of residence through combined molecular analyses[11,14–16]. Human ILCs are actively studied in the tonsils[14,17–19], skin[20], gastrointestinal[13] and respiratory tracts[12], but remain largely uncharacterized in the FGT. Helper ILCs have been described to a limited extent in the human endometrium (EM) and decidua during pregnancy[21,22], but their role in mucosal protection throughout the non-pregnant FGT remains unknown. Studies of blood, gut and tonsils from patients infected with HIV have described ILC alterations in the context of chronic infection[18,23,24]; however, the genital mucosa, a major site for HIV infection, has not been investigated[25]. Importantly, the role that ILCs have in mucosal HIV pathogenesis immediately after exposure, and whether they can respond to HIV stimulation, is completely unknown.

The immune system in the FGT is different from other mucosal surfaces, as it is uniquely conditioned and regulated by sex hormones to perform reproductive functions and protect against pathogens[7]. Each anatomical region of the FGT exhibits discrete histological, immunological and functional traits. The lower FGT, consisting of the ectocervix (ECT) and vagina, is covered by stratified squamous epithelial cells, populated by commensal microbes and serves as the area of semen reception[7]. By contrast, the upper FGT, which includes the uterine endocervix (END) and endometrium (EM), is lined with a single layer of columnar epithelium, has fewer commensal microbes and is specialized to facilitate embryo implantation and pregnancy[7].

Previously, we demonstrated immune compartmentalization of T cell populations throughout the FGT, including differences in T_H17 CD4$^+$ T cell distribution and susceptibility to HIV infection[26–29], emphasizing the importance of studying the entire FGT. Defining how—throughout the FGT—ILCs maintain tissue homeostasis in a mucosa dually tasked with pathogen protection and reproduction, along with their response to HIV, will fill a gap in knowledge of mucosal defense against pathogens and open new avenues for therapeutic interventions.

Here we used a multi-omics approach with high-dimensional flow cytometry, CITE-seq and ChipCytometry to deeply characterize the distribution and spatial location of helper ILCs throughout the human FGT, including the EM, END and ECT. Moreover, we defined the ability of ILCs to respond to HIV challenge in a subset-specific manner, suggesting a role for genital ILCs in mucosal antiviral responses.

Results

ILCs reside in the female genital mucosa and are armed with antiviral cytokines at homeostasis

ILC presence and subset distribution under homeostatic conditions throughout the FGT remain uncharacterized. To address this knowledge gap, we assessed ILC subsets using high-dimensional spectral flow cytometry. Genital ILCs were identified as CD45$^+$ cells that lacked canonical lineage markers (CD3, CD19, CD11b, CD14, CD16, CD66b, CD11c) and expressed CD127 (IL-7R) (Fig. 1a), according to established definitions in other human mucosal surfaces. Our gating strategy excluded canonical natural killer (NK) cells, determined by lack of expression of NKp46 (CD335) and CD94 on ILCs, and lack of CD127 expression on NK cells[9] (Extended Data Fig. 1a,b). Additionally, NK cells expressed high levels of CD56 and CD94, whereas helper ILCs expressed low levels of CD56 throughout the FGT (Extended Data Fig. 1c,d). Our strategy excluded other rare cell types that may contaminate the ILC gate. We did not detect CD203c expression (a marker of mast cells and basophils[30]), CD34$^+$ progenitor cells or CD123$^+$ plasmacytoid dendritic cells (Extended Data Fig. 1e–g).

ILCs represented approximately 0.52% of the total mononuclear immune cells, with no differences between tissues, and the number of ILCs per gram of tissue was significantly higher in EM than in ECT (Fig. 1b).

Next, we quantified genital ILC subsets, according to the expression of CD294 (ILC2s), CD117 (ILC3s) or double-negative populations (ILC1s) as previously described[10] (Fig. 1c). ILC1s and ILC3s were the main subsets present but showed compartmentalization, with ILC1s enriched in the END and ECT, while ILC3s were enriched within the EM (Fig. 1d). ILC2s displayed very low frequencies throughout the FGT (Fig. 1d), with more than half of the patients having less than 5% or no ILC2s (Fig. 1e). Genital T cells (CD3$^+$) from the same samples displayed high CD294 expression (Extended Data Fig. 1h), demonstrating that the lack of CD294 expression on ILCs was a result of low ILC2 presence in genital tissues and not caused by faulty antibody staining. ILC3s displayed higher CD127 expression than ILC1s (Extended Data Fig. 1i).

Next, we assessed canonical transcription factor expression: T-bet (ILC1s), GATA-3 (ILC2s) and RORγt (ILC3s)[10]. ILC1s (CD294$^-$CD117$^-$) expressed T-bet, ILC2s (CD294$^+$) expressed GATA-3 and ILC3s (CD117$^+$) expressed RORγt (Fig. 1f). Approximately 80% of ILC1s were T-bet$^+$, 95% of ILC2s were GATA-3$^+$ and 98% of ILC3s were RORγt$^+$, consistently across samples (Fig. 1g). Our transcription factor expression patterns identified a small population of ILC1-like cells that do not express T-bet (Fig. 1f,g), similar to recent findings in other human mucosal surfaces[19].

Lastly, we investigated cytokine production to define the functional status of ILCs in the genital mucosa under homeostatic conditions. In the absence of stimulation, intracellular staining showed IFNγ production by genital ILC1s (Fig. 1h; CD117$^-$) and IL-22 by ILC3s (Fig. 1i; CD117$^+$). IFNγ$^+$ ILC1s and IL-22$^+$ ILC3s represented about 10% and 45%, respectively, of each ILC subset across all tissues (Fig. 1h,i). Given that most immune cells do not constitutively produce IFNγ or IL-22, we compared cytokine expression in ILCs to unstimulated NK cells and T cells from the same tissues. Interestingly, we observed that genital ILCs were the main producers of IFNγ and IL-22 under homeostatic conditions (Fig. 1j,k). Of note, genital ILCs did not constitutively produce IL-17, IL-5, IL-13 or NK-related cytolytic molecules such as Granulysin (Extended Data Fig. 1j,k).

In summary, genital ILC subsets are compartmentalized and loaded with specific antiviral cytokines under homeostatic conditions, suggesting potential roles in first-line antiviral mucosal protection.

Fig. 1 | ILC subsets reside in the female genital mucosa in a compartment-specific distribution and are armed with antiviral cytokines at homeostasis. a, Representative gating strategy to identify genital lineage-negative, CD127$^+$ ILCs. SSC-A, side scatter area; FSC-A, forward scatter area; FSC-H, forward scatter height; FMO, fluorescence minus one. **b**, Quantification of ILC percentage in EM (*n* = 26), END (*n* = 18) and ECT (*n* = 16) per total mononuclear cells and ILC number per gram of tissue (EM, *n* = 22; END, *n* = 17; ECT, *n* = 15 tissues). **c**, Contour plot showing ILC subset gating strategy. **d**, Comparison of percentage of ILC subsets in total ILCs across three tissues (*n* = 56). **e**, Pie charts indicating the percentage of patients with 0, <5% or >5% ILC2s in total ILCs (EM, *n* = 25; END, *n* = 16; ECT, *n* = 15). **f**, Contour plot showing ILC subsets along with matching histograms of transcription factor expression within the gated ILC subsets. **g**, Representative contour plots indicating percentage of ILC1s, ILC2s and ILC3s positive for T-bet, GATA-3 and RORγt, respectively. The FMO strategy was used to determine positive gates. Quantification of multiple donors (right): T-bet (*n* = 6), GATA-3 (*n* = 4) and RORγt (*n* = 4). **h**,**i**, Contour plot and quantification of IFNγ (*n* = 45 tissues: EM, *n* = 18; END, *n* = 10; ECT, *n* = 17) (**h**) and IL-22 expression in genital ILCs (*n* = 36 tissues: EM, *n* = 16; END, *n* = 9; ECT, *n* = 11) (**i**). **j**,**k**, Histogram of IFNγ (**j**) and IL-22 (**k**) expression in ILCs, CD3$^+$ T cells, CD56^{hi}CD127$^-$ NK cells and FMO. Each dot represents a biological replicate. Horizontal lines represent the median ± interquartile range (IQR). Statistical analysis was performed using the non-parametric Kruskal–Wallis test with Dunn's post-test correction for multiple comparisons.

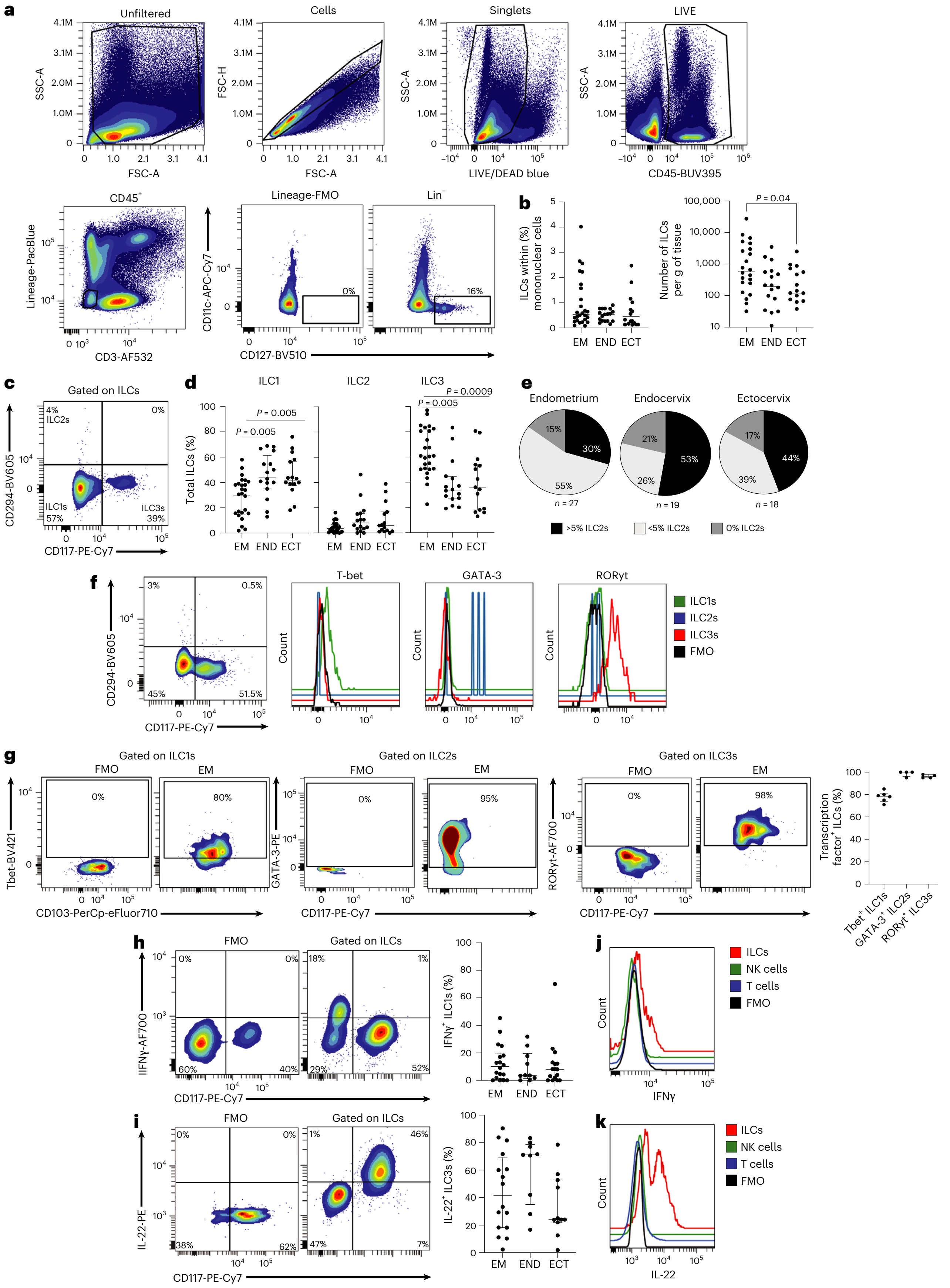
a
Unfiltered
Cells
Singlets
LIVE
SSC-A
FSC-H
FSC-A
LIVE/DEAD blue
CD45-BUV395
4.1M
3.1M
2.0M
1.0M
0
1.0
2.1
3.1
4.1
-10^4
10^4
10^5
10^6
CD45$^+$
Lineage-FMO
Lin$^-$
Lineage-PacBlue
CD3-AF532
CD11c-APC-Cy7
CD127-BV510
0%
16%
b
ILCs within (%) mononuclear cells
Number of ILCs per g of tissue
P = 0.04
EM END ECT
c
Gated on ILCs
CD294-BV605
CD117-PE-Cy7
4% ILC2s
0%
ILC1s 57%
ILC3s 39%
d
ILC1
ILC2
ILC3
Total ILCs (%)
P = 0.005
P = 0.005
P = 0.0009
P = 0.005
e
Endometrium
Endocervix
Ectocervix
15%
30%
55%
n = 27
21%
53%
26%
n = 19
17%
44%
39%
n = 18
■ >5% ILC2s
□ <5% ILC2s
▨ 0% ILC2s
f
3%
0.5%
45%
51.5%
T-bet
GATA-3
RORγt
Count
ILC1s
ILC2s
ILC3s
FMO
g
Gated on ILC1s
Gated on ILC2s
Gated on ILC3s
FMO
EM
Tbet-BV421
CD103-PerCp-eFluor710
GATA-3-PE
RORγt-AF700
0%
80%
0%
95%
0%
98%
Transcription factor$^+$ ILCs (%)
Tbet$^+$ ILC1s
GATA-3$^+$ ILC2s
RORγt$^+$ ILC3s
h
FMO
Gated on ILCs
IFNγ-AF700
0%
0%
60%
40%
18%
1%
29%
52%
IFNγ$^+$ ILC1s (%)
i
IL-22-PE
0%
0%
38%
62%
1%
46%
47%
7%
IL-22$^+$ ILC3s (%)
j
ILCs
NK cells
T cells
FMO
IFNγ
k
IL-22

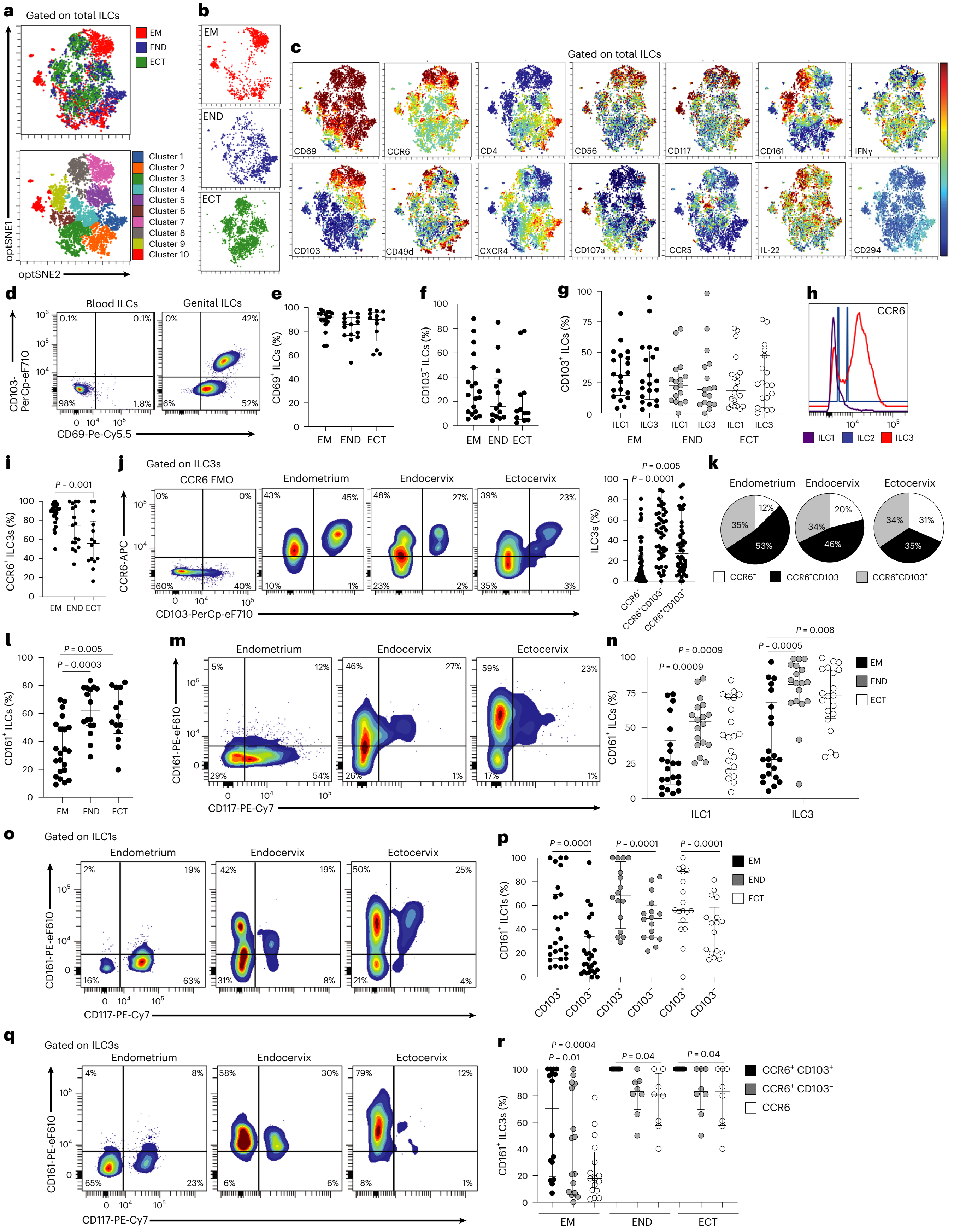
a
Gated on total ILCs
EM
END
ECT
Cluster 1
Cluster 2
Cluster 3
Cluster 4
Cluster 5
Cluster 6
Cluster 7
Cluster 8
Cluster 9
Cluster 10
optSNE1
optSNE2
b
EM
END
ECT
c
Gated on total ILCs
CD69
CCR6
CD4
CD56
CD117
CD161
IFNγ
CD103
CD49d
CXCR4
CD107a
CCR5
IL-22
CD294
d
Blood ILCs
Genital ILCs
0.1%
0.1%
98%
1.8%
0%
42%
6%
52%
CD103-PerCp-eF710
CD69-Pe-Cy5.5
e
CD69+ ILCs (%)
EM END ECT
f
CD103+ ILCs (%)
EM END ECT
g
CD103+ ILCs (%)
ILC1 ILC3 ILC1 ILC3 ILC1 ILC3
EM END ECT
h
CCR6
ILC1
ILC2
ILC3
i
P = 0.001
CCR6+ ILC3s (%)
EM END ECT
j
Gated on ILC3s
CCR6 FMO
Endometrium
Endocervix
Ectocervix
0%
0%
60%
40%
43%
45%
10%
1%
48%
27%
23%
2%
39%
23%
35%
3%
CCR6-APC
CD103-PerCp-eF710
P = 0.005
P = 0.0001
ILC3s (%)
CCR6−
CCR6+CD103−
CCR6+CD103+
k
Endometrium
Endocervix
Ectocervix
12%
35%
53%
20%
34%
46%
34%
31%
35%
CCR6−
CCR6+CD103−
CCR6+CD103+
l
P = 0.005
P = 0.0003
CD161+ ILCs (%)
EM END ECT
m
Endometrium
Endocervix
Ectocervix
5%
12%
29%
54%
46%
27%
26%
1%
59%
23%
17%
1%
CD161-PE-eF610
CD117-PE-Cy7
n
P = 0.0009
P = 0.0009
P = 0.008
P = 0.0005
CD161+ ILCs (%)
ILC1
ILC3
EM
END
ECT
o
Gated on ILC1s
Endometrium
Endocervix
Ectocervix
2%
19%
16%
63%
42%
19%
31%
8%
50%
25%
21%
4%
CD161-PE-eF610
CD117-PE-Cy7
p
P = 0.0001
P = 0.0001
P = 0.0001
CD161+ ILC1s (%)
CD103+
CD103−
CD103+
CD103−
CD103+
CD103−
EM
END
ECT
q
Gated on ILC3s
Endometrium
Endocervix
Ectocervix
4%
8%
65%
23%
58%
30%
6%
6%
79%
12%
8%
1%
CD161-PE-eF610
CD117-PE-Cy7
r
P = 0.0004
P = 0.01
P = 0.04
P = 0.04
CD161+ ILC3s (%)
EM
END
ECT
CCR6+ CD103+
CCR6+ CD103−
CCR6−

Fig. 2 | Unbiased clustering reveals discriminatory markers of genital ILC subsets and markers of tissue residency. **a**, opt-SNE plots on concatenated total ILCs from three matched patients' EM, END and ECT samples (top). FlowSOM clustering analysis overlayed onto the opt-SNE plot with ten distinct clusters (bottom). **b**, opt-SNE plot of total ILCs from three patients split by anatomical region. **c**, opt-SNE plot of total ILCs with individual protein expression overlayed. The color determines the intensity of expression (blue, low; red, high). **d**, Contour plot of CD103 and CD69 expression in blood and genital ILCs. **e**,**f**, Quantification of the percentage of CD69 (**e**) and CD103 (**f**) expressing genital ILCs. **g**, Quantification of the percentage of CD103$^+$ ILCs by subset across tissues (*n* = 56 tissues). **h**, Representative histogram of CCR6 expression in each ILC subset. **i**, Quantification of CCR6 expression in ILC3s. **j**, Contour plot of CD103 and CCR6 expression in ILC3s (left) with CCR6 FMO. Quantification of ILC3 subsets in all tissues (right). **k**, Pie graph of the percentage of ILC3 subsets in total ILC3s. **l**, Percentage of CD161$^+$ ILCs in each tissue. **m**, Contour plot of CD161 expression. **n**, Percentage of CD161$^+$ ILC1s and ILC3s in the EM, END and ECT. **o**, Contour plot of CD161 and CD103 expression in ILC1s. **p**, Percentage of CD161$^+$ ILC1s in CD103$^+$ and CD103$^-$ ILC1s. **q**, Contour plot of CD161 and CD103 expression in ILC3s. **r**, Percentage of CD161$^+$ ILC3s in CCR6$^+$CD103$^+$, CCR6$^+$CD103$^-$ and CCR6$^-$ ILC3s. Each dot represents a biological replicate; *n* = 61 tissues. Horizontal lines represent the median ± IQR. Statistical analysis was performed using the non-parametric Kruskal–Wallis test with Dunn's post hoc test correction for multiple comparisons.

Unbiased clustering reveals discriminatory markers of genital ILC subpopulations and markers of tissue residency

To further uncover discriminatory markers that define functional ILC subpopulations, we performed unbiased clustering of high-dimensional flow cytometry data.

Genital ILCs clustered closely based on tissue type (Fig. 2a, upper panel). Individual clustering per patient is shown in Extended Data Fig. 2a. ILCs from the EM (Fig. 2a,b, red) clustered more independently than ILCs from the END and ECT (Fig. 2a,b, blue and green), suggesting that endometrial ILCs are phenotypically more distinct than cervical ILCs.

Next, to uncover genital ILC subpopulations, we used unsupervised clustering analysis (FlowSOM) to perform multivariate clustering of cells based on self-organized maps. ILCs were grouped into ten clusters that were overlayed on the opt-SNE plots (Fig. 2a, lower panel). This analysis identified tissue-dependent clusters, such as cluster 7 or 9, while others were intermixed (cluster 5 or 3) (Fig. 2a). To identify key drivers of clustering, we overlaid individual proteins on the opt-SNE plots (Fig. 2c). Most ILCs expressed high levels of CD69, a marker for tissue residency. Analysis of protein expression in each cluster identified surface markers that revealed anatomical differences, like CD161 and CXCR4 (Fig. 2c), and initial assignment of clusters to specific ILC subsets (Extended Data Fig. 2b). We also identified discriminatory markers for exploration of specific ILC clusters, mainly CD103, CCR6, CD161 and CD107a (Fig. 2a–c and Extended Data Fig. 2c). Importantly, stratification of functional markers (IFNγ, IL-22 and CD107a) per individual patient and by tissue revealed tissue-specific differences and patient-to-patient variation (Extended Data Fig. 2d), indicating the need for further evaluation in a larger cohort.

Therefore, we validated our findings with a larger number of patients (*n* = 32). The majority of genital ILCs expressed CD69 (Fig. 2d), with no differences between anatomical sites (Fig. 2e). Additionally, a proportion of CD69$^+$ ILCs co-expressed CD103 (Fig. 2d) with no differences between anatomical sites (Fig. 2f) or ILC subsets (ILC1, ILC3) (Fig. 2g). ILC2s were excluded from these analyses because of low cell number and absence of this population in a large proportion of patients (Fig. 1c,d).

Our unbiased clustering analysis indicated high levels of co-expression between CD103 and CCR6, a chemokine receptor for CCL20, which is produced by genital epithelial cells[31]. CCR6 was highly expressed on ILC3s (Fig. 2h) and preferential to the EM (Fig. 2i). The majority of CD103$^+$ ILC3s co-expressed CCR6 (Fig. 2j), allowing the discrimination of three unique ILC3 subpopulations based on CD103 and CCR6 expression: CCR6$^-$, CCR6$^+$CD103$^-$ and CCR6$^+$CD103$^+$ ILC3s (Fig. 2j). A representative dot plot of CCR6 versus CD45 expression and corresponding fluorescence-minus-one control is shown to clarify the gating strategy (Extended Data Fig. 2e). Quantification of each ILC3 subset across the FGT showed enrichment of CCR6$^-$ in ECT and CCR6$^+$CD103$^-$ in the EM, while the CCR6$^+$CD103$^+$ population remained constant across tissues (Fig. 2k).

CD161, a site-specific discriminatory marker identified in the opt-SNE plot, showed significant differential expression between endometrial and cervical ILCs (Fig. 2l,m) but similar expression between ILC1s and ILC3s (Fig. 2n). Furthermore, CD161 was preferentially co-expressed on CD103$^+$ ILC1s and ILC3s (Fig. 2o–q), particularly on the CD103$^+$CCR6$^+$ ILC3 subpopulations in the END and ECT (Fig. 2r).

CD161 and NKp44 discriminate functional ILC subsets at homeostasis

We next investigated potential associations between phenotypical markers (CD103, CD161 and CCR6) and functional specialization of ILC subsets. IFNγ production by ILC1s was independent of CD103 expression (Fig. 3a and Extended Data Fig. 3a), but significantly enhanced in CD161$^-$ ILC1s (Fig. 3b and Extended Data Fig. 3b). IL-22 production was highest in CCR6$^+$CD103$^+$ ILC3s compared to CCR6$^+$CD103$^-$ and CCR6$^-$ ILC3s (Fig. 3c and Extended Data Fig. 3c). Furthermore, CD161$^+$ ILC3s displayed enhanced IL-22 production (Fig. 3d and Extended Data Fig. 3d). These data suggest that CD161 is a relevant marker to discriminate ILC subsets with high cytokine production at homeostasis.

We next investigated ILC degranulation (CD107a expression) as an additional functional parameter detected in our unbiased

Fig. 3 | CD161 and NKp44 discriminate functional ILC subsets at homeostasis. **a**, Representative histogram (left) and contour plot (middle) of IFNγ expression in CD103$^+$ and CD103$^-$ ILC1s with quantification of percentage of IFNγ$^+$ ILC1s (right) (*n* = 30). **b**, Histogram and contour plot of IFNγ expression in CD161$^+$ and CD161$^-$ ILC1s (left) (*n* = 30). Quantification of IFNγ$^+$CD103$^-$ and CD103$^+$ ILC1s based on CD161 expression (right). **c**, Histogram and contour plot of IL-22 expression in ILC3 subsets (left) with quantification of percentage of IL-22$^+$ ILC3 subsets (right) (*n* = 30). **d**, Histogram and contour plot of IL-22 expression in CD161$^+$ and CD161$^-$ ILC3s. Quantification of IL-22$^+$CCR6$^+$CD103$^+$ and CCR6$^+$CD103$^-$ ILC3s based on CD161 expression (right) (*n* = 30). **e**, Representative contour plot of CD107a expression in FMO (left) and EM (right) ILCs. **f**, Histogram of CD107a expression in ILCs, NK cells and T cells. **g**, Contour plot of CD107a and CD117 in total ILCs. **h**, Contour plot of CD103 and CD107a in ILC3s. **i**, Histogram and contour plot of CD107a expression in all ILC subsets. **j**, Percentage of CD107a$^+$ cells by ILC3 subsets. **k**, Percentage of CD107a$^+$CCR6$^+$CD103$^-$ ILC3s by tissue (*n* = 24 tissues). **l**, Contour plot of CD161 and CD107a expression (left) and mean fluorescence intensity (MFI) comparison between CD107a$^+$ and CD107a$^-$ in *n* = 12 EM samples. **m**, Contour plot of NKp44 and CD117 (left) and percentage of NKp44$^+$ ILC3s by tissue (right) (*n* = 17 tissues: EM, *n* = 7; END, *n* = 5; ECT, *n* = 5). **n**, Representative histogram of NKp44 expression in ILC subsets (left). Percentage of NKp44$^+$ ILC3s by ILC3 subset (right) (*n* = 9 tissues). **o**, Contour plot of CD107a and NKp44 expression in EM (top) and END (middle) ILC3s. Percentage of NKp44$^+$ ILC3s that are CD107a$^+$ (bottom) (*n* = 10 tissues: EM, *n* = 5; END and ECT, *n* = 5). **p**, Contour plots representing IL-22 secretion during PMA stimulation for 1 h in NKp44$^{+/-}$ ILC3s. Graph on the right represents the percentage of ILC3s positive for IL-22 secretion with and without stimulation (*n* = 6 tissues). **q**, Representative contour plots of CD107a expression in genital NKp44$^{+/-}$ ILC3s with and without PMA stimulation. Graph on the right represents the percentage of ILC3s positive for CD107a with and without stimulation (*n* = 6). Each dot represents a biological replicate. Horizontal lines represent the median ± IQR. Statistical analysis was performed using the non-parametric Kruskal–Wallis test with Dunn's post hoc test correction for multiple comparisons.

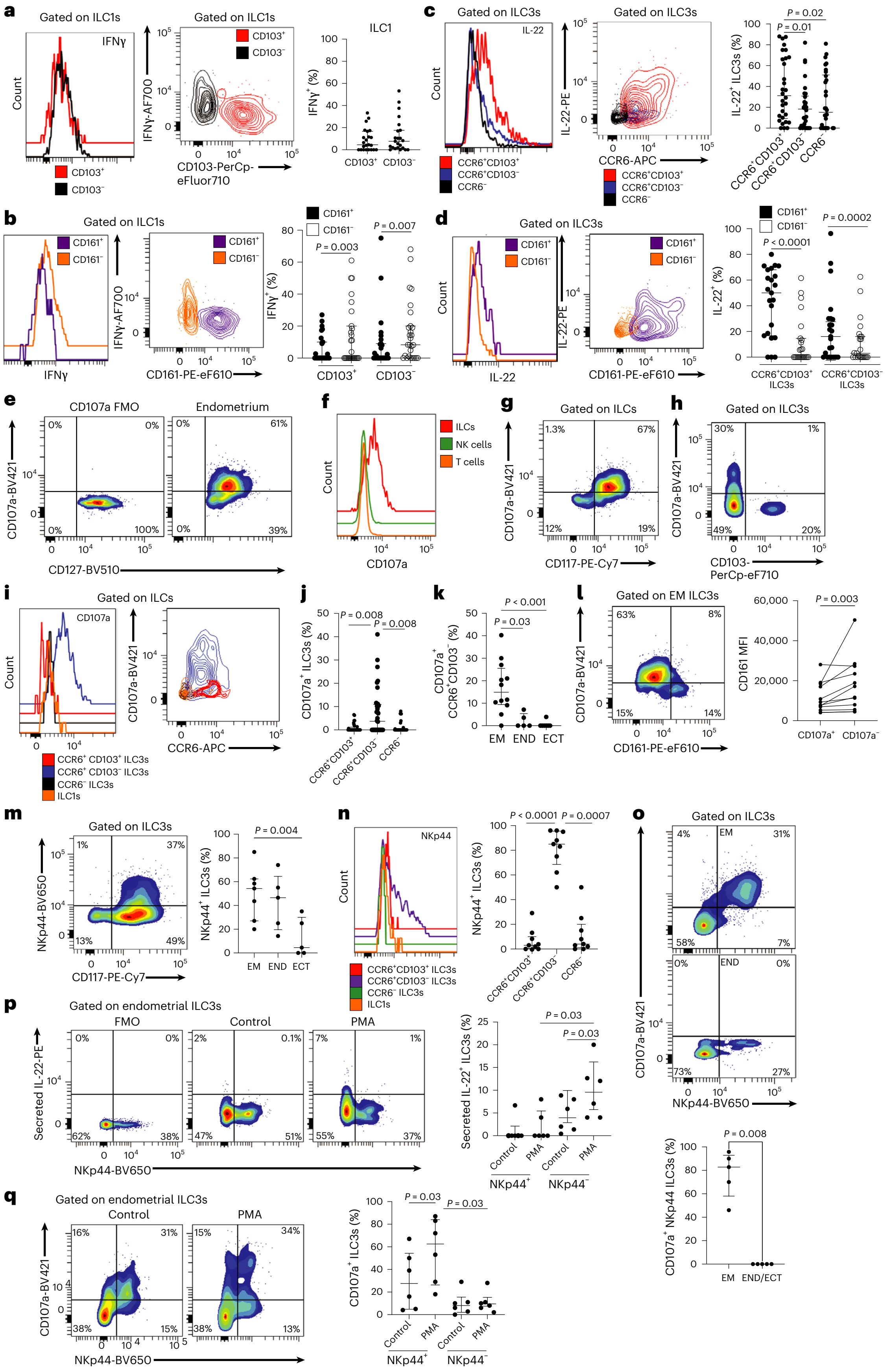
a
Gated on ILC1s
IFNγ
Count
CD103+
CD103−
Gated on ILC1s
IFNγ-AF700
CD103-PerCp-eFluor710
ILC1
IFNγ+ (%)
c
Gated on ILC3s
IL-22
CCR6+CD103+
CCR6+CD103−
CCR6−
IL-22-PE
CCR6-APC
P = 0.02
P = 0.01
IL-22+ ILC3s (%)
b
Gated on ILC1s
CD161+
CD161−
IFNγ-AF700
CD161-PE-eF610
P = 0.007
P = 0.003
IFNγ+ (%)
d
Gated on ILC3s
P = 0.0002
P < 0.0001
IL-22+ (%)
IL-22-PE
CCR6+CD103+ ILC3s
CCR6+CD103− ILC3s
e
CD107a FMO
Endometrium
CD107a-BV421
CD127-BV510
f
ILCs
NK cells
T cells
CD107a
g
Gated on ILCs
CD117-PE-Cy7
h
Gated on ILC3s
CD103-PerCp-eF710
i
Gated on ILCs
CD107a
CCR6+ CD103+ ILC3s
CCR6+ CD103− ILC3s
CCR6− ILC3s
ILC1s
CCR6-APC
j
P = 0.008
P = 0.008
CD107a+ ILC3s (%)
k
P < 0.001
P = 0.03
CD107a+ CCR6+CD103− (%)
EM
END
ECT
l
Gated on EM ILC3s
CD161-PE-eF610
P = 0.003
CD161 MFI
CD107a+
CD107a−
m
Gated on ILC3s
NKp44-BV650
CD117-PE-Cy7
P = 0.004
NKp44+ ILC3s (%)
n
NKp44
CCR6+CD103+ ILC3s
CCR6+CD103− ILC3s
CCR6− ILC3s
ILC1s
P < 0.0001
P = 0.0007
NKp44+ ILC3s (%)
o
Gated on ILC3s
EM
END
CD107a-BV421
NKp44-BV650
P = 0.008
CD107a+ NKp44 ILC3s (%)
END/ECT
p
Gated on endometrial ILC3s
FMO
Control
PMA
Secreted IL-22-PE
NKp44-BV650
P = 0.03
P = 0.03
Secreted IL-22+ ILC3s (%)
NKp44+
NKp44−
q
Gated on endometrial ILC3s
Control
PMA
CD107a-BV421
NKp44-BV650
P = 0.03
P = 0.03
CD107a+ ILC3s (%)

analysis (Fig. 2c). Although CD107a is normally expressed on the cell surface following stimulation, we detected CD107a expression on a high percentage of genital ILCs in the absence of in vitro stimulation (Fig. 3e). Importantly, CD107a expression was limited to ILCs, while genital T cells and NK cells from the same unstimulated samples did not express CD107a (Fig. 3f). Further analysis demonstrated that degranulation was specific for ILC3s (CD117$^+$; Fig. 3g), and particularly CCR6$^+$CD103$^-$ ILC3s (Fig. 3h–j and Extended Data Fig. 3e). However, degranulation occurred primarily in the EM, with little to no CD107a expression in the END and ECT (Fig. 3k). Given that CD161 identified ILC3s with high intracellular IL-22 (Fig. 3d), we assessed whether CD161 expression was also related to degranulation. However, endometrial CD107a$^+$ ILC3s expressed significantly lower levels of CD161 (Fig. 3l).

As we observed a wide range of IL-22, IFNγ and CD107a expression between patients, we investigated whether cytokine production and degranulation could identify patients with 'highly functional' ILCs. We performed correlations between IL-22, IFNγ and CD107a across patients; however, we did not detect any correlations (Extended Data Fig. 3f), suggesting that ILC subsets function independently of each other under homeostatic conditions.

To better define the ILC3 degranulating population, we evaluated NKp44 expression, previously described in intestinal[32], endometrial and decidual ILCs[21,22]. NKp44 was exclusively expressed on ILC3s (CD117$^+$) and was present throughout the FGT, although significantly enriched in the EM (Fig. 3m). NKp44 expression was specific to CCR6$^+$CD103$^-$ ILC3s (Fig. 3n), the same subset undergoing degranulation (Fig. 3i,j). Consistently, NKp44$^+$ ILC3s co-expressed CD107a and were found primarily at the EM (Fig. 3o), indicating ongoing endometrial ILC3 degranulation at homeostasis. To explore whether the NKp44$^+$ and NKp44$^-$ ILC3 subsets were able to rapidly secrete the IL-22 stored intracellularly, and degranulate in response to stimulation, we performed a flow-cytometry-based IL-22 secretion assay. A small percentage of ILC3s secreted IL-22 under resting conditions (Fig. 3p, control), but IL-22 secretion was significantly increased in response to phorbol 12-myristate-13-acetate (PMA) stimulation (Fig. 3p, PMA). Moreover, NKp44$^-$ ILC3s secreted IL-22 in response to PMA stimulation (Fig. 3p), while NKp44$^+$ ILC3s significantly upregulated CD107a expression after stimulation (Fig. 3q), indicating different functionalities between these two ILC3 subsets.

NKp44$^+$ ILC3s reside in lymphoid aggregates within the EM

Our data indicate the presence of multiple ILC subpopulations within the tissue, each with distinct functional phenotypes. Given that ILCs are known to interact with the tissue environment and regulate other cell types, we investigated the spatial location and cell interactions of genital ILCs to understand the functional consequences for these distinct phenotypes. As ILCs lack canonical lineage markers and are difficult to accurately identify with conventional confocal microscopy, we used ChipCytometry to achieve multiplexed spatial fluorescence microscopy. Building on our flow cytometry data, we identified ILCs as lineage-negative (CD3, CD20, CD11c, CD14, CD16, CD66b) CD127$^+$ cells (Extended Data Fig. 4a) and visualized functional ILC subpopulations through the expression of CD117, CCR6, CD103, CD161 and NKp44 (Extended Data Fig. 4a).

In the EM, we identified ILCs positioned within large clusters of CD45$^+$ cells located near endometrial epithelial glands (Fig. 4a). These cell aggregates consisted largely of lymphocytes, including CD3$^+$ T cells and CD20$^+$ B cells. Within the lymphoid aggregates, we exclusively found ILC3s (CD117$^+$) co-expressing CCR6 and NKp44 (Fig. 4a,b). We identified both CD161$^+$ and CD161$^-$ NKp44$^+$ ILC3s in the aggregates, closely interacting with CD4$^+$ and CD4$^-$ T cells (CD3$^+$), and B cells (CD20$^+$) (Fig. 4b). Additionally, we observed clusters of NKp44$^+$ ILC3s (CD161$^+$ and CD161$^-$) localizing to the edge of the glands present in the EM, interacting closely with epithelial cells (PanCk$^+$) (Fig. 4c). We did not find NKp44$^-$ ILC3s within the aggregates (Fig. 4a–c). We identified CCR6$^+$NKp44$^-$ ILC3s positioned close to endometrial epithelial glands, interacting with CD45$^-$ stromal cells but not in contact with T cells or B cells (Fig. 4d). To quantify the NKp44$^+$ and NKp44$^-$ ILC3 subsets, we selected regions of interest with ILC3s that contained lymphoid aggregates and those that did not (Extended Data Fig. 4b). In these regions, we counted the number of NKp44$^{+/-}$ ILC3s per area. The majority of NKp44$^-$ ILC3s were located outside of lymphoid aggregates, while almost all NKp44$^+$ ILC3s were found in the lymphoid aggregates (Fig. 4e).

In the ECT, we primarily detected ILC1s (Fig. 4f,g). In contrast to the EM, the ILCs identified in the ECT did not cluster together and were not located within cell aggregates. CD161$^+$ and CD161$^-$ ILC1s were present close to the stratified ectocervical epithelium and preferentially interacted with T cells (Fig. 4f,g). CD103$^+$ ILC1s were located closer to the basal layer of the stratified epithelium (Fig. 4g). To quantify ILC1 subsets (CD161$^+$, CD161$^-$ and CD103$^+$) in the ECT, we selected areas of interest based on tissue location relative to the epithelium (intraepithelial, subepithelial and deeper tissue; Extended Data Fig. 4c). ILC1s were located in the subepithelial or deeper tissue compartments, while no ILC1s were found within the epithelium (Fig. 4h). Furthermore, CD103$^+$ and CD161$^-$ ILC1s were preferentially located in the subepithelial compartment, while CD161$^+$ ILC1s were more abundant deeper in the tissue and did not express CD103 (Fig. 4h).

Our data indicate that the functional markers CD103, CD161 and NKp44 also associate with ILC spatial location and potential cell interactions.

Genital ILC subsets are regulated by age and prior pregnancies

Given that we observed anatomical compartmentalization and high donor-to-donor variability in genital ILC distribution and phenotype, we investigated whether ILCs are modified according to age and reproductive parameters. To determine age-associated effects on ILCs, we performed correlation analyses. As women age, the percentage of ILCs in total mononuclear cells decreases in ECT but remains unchanged in EM and END (Fig. 5a). However, ILC subset analysis showed an age-dependent switch in subset distribution in the EM specifically, with a reduction in ILC1 percentage (Fig. 5b) concomitant with an ILC3 increase (Fig. 5c), while ILC subset distribution in the END and ECT was not affected by age (Fig. 5b,c). Given these differential effects in the EM, we investigated whether prior pregnancies affected ILC frequency. First, we compared donors who were never pregnant to donors who had at least one pregnancy, but no differences were found (Fig. 5d). However, we observed that time after last pregnancy positively correlated with ILC percentage in the EM. Donors who were recently pregnant had

Fig. 4 | NKp44$^+$ ILC3s reside in lymphoid aggregates within the EM. **a**, Representative image of lymphoid aggregates in the EM (top) and zoomed in (bottom). PanCK (white) identifies epithelial cells; DAPI (blue) identifies nuclei. **b**, Representative image of NKp44$^+$ ILC3s at 10 μm. Images are separated by channels. Red arrows denote CD161$^+$ ILC3s; white arrows denote CD161$^-$ ILC3s. **c**, Zoomed-in image of NKp44$^+$ ILC3s in the aggregate near PanCK$^+$ cells. **d**, NKp44$^-$ ILC3 in the EM. **e**, Quantification of NKp44$^+$ and NKp44$^-$ ILC3s per area ($\log_{10}$ scale) in regions of interest (ROIs) that contained ILC3s: lymphoid aggregates (LA; $n = 5$ ROIs) and non-lymphoid aggregates (non-LA; $n = 15$ ROIs). Horizontal lines represent the median ± IQR. **f**, CD103$^-$CD161$^+$ ILC1s in the ECT. **g**, CD103$^+$CD161$^-$ ILC1s in the END near the epithelium; $n = 3$ donors, with nine tissues total (EM, END and ECT for each). **h**, Number of CD161$^+$, CD161$^-$ and CD103$^+$ ILC1s per area ($\log_{10}$ scale) in ROIs containing ILCs: intraepithelial ($n = 3$ ROIs including the entirety of the epithelium from three patients), subepithelial ($n = 5$ ROIs) and deeper tissue ($n = 7$ ROIs). Each dot represents one ROI. ROIs from three patients were used. Horizontal lines represent the median ± IQR. Kruskal–Wallis test with Dunn's post hoc test correction for multiple comparisons.

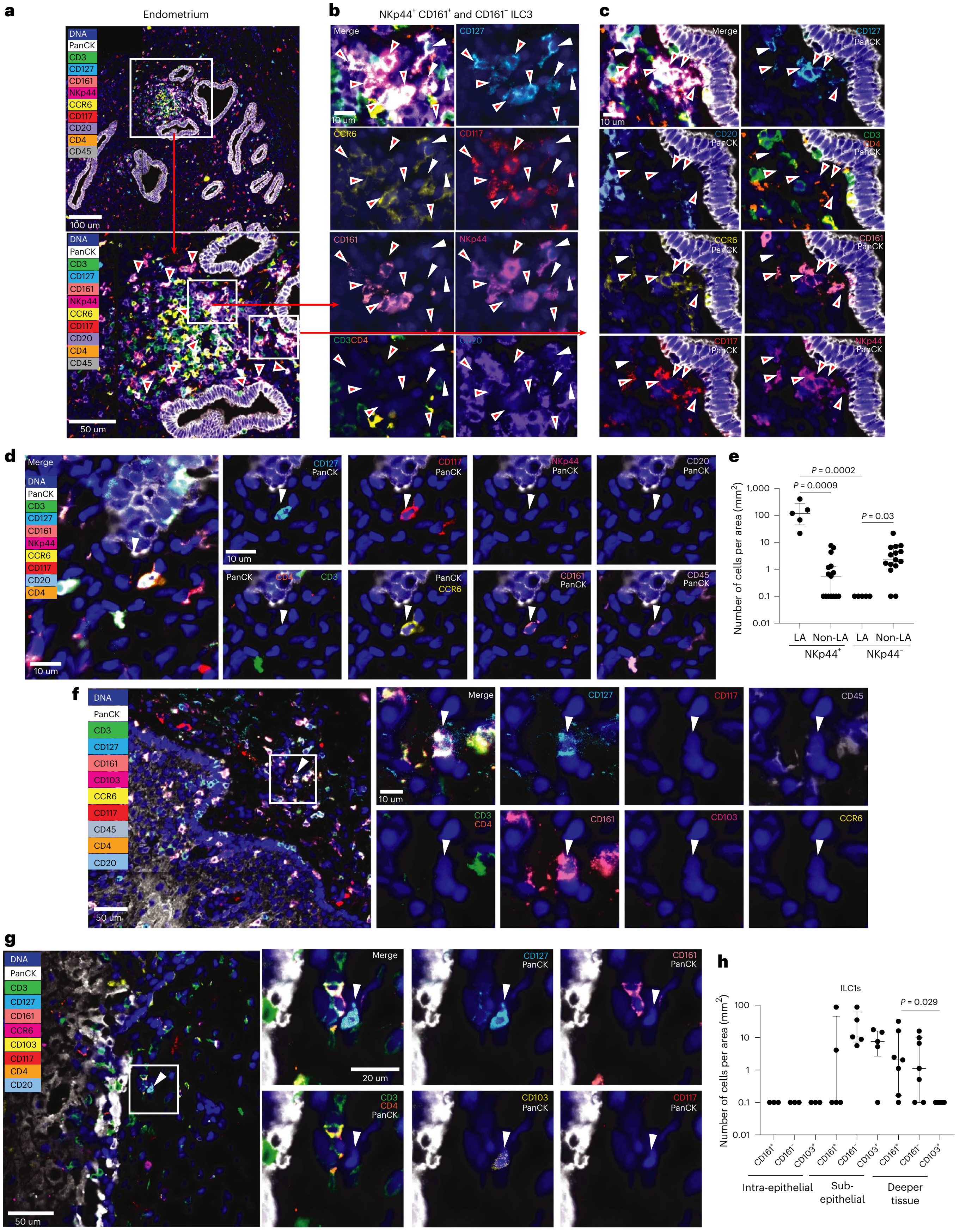
a
Endometrium
DNA
PanCK
CD3
CD127
CD161
NKp44
CCR6
CD117
CD20
CD4
CD45
100 um
50 um
b
NKp44+ CD161+ and CD161− ILC3
Merge
CD127
CCR6
CD117
CD161
NKp44
CD3 CD4
CD20
10 um
c
Merge
CD127 PanCK
CD20 PanCK
CD3 CD4 PanCK
CCR6 PanCK
CD161 PanCK
CD117 PanCK
NKp44 PanCK
10 um
d
Merge
DNA
PanCK
CD3
CD127
CD161
NKp44
CCR6
CD117
CD20
CD4
CD127 PanCK
CD117 PanCK
NKp44 PanCK
CD20 PanCK
PanCK CD4 CD3
PanCK CCR6
CD161 PanCK
CD45 PanCK
10 um
e
P = 0.0002
P = 0.0009
P = 0.03
Number of cells per area (mm2)
1,000
100
10
1
0.1
0.01
LA
Non-LA
LA
Non-LA
NKp44+
NKp44−
f
DNA
PanCK
CD3
CD127
CD161
CD103
CCR6
CD117
CD45
CD4
CD20
50 um
Merge
CD127
CD117
CD45
CD3 CD4
CD161
CD103
CCR6
10 um
g
DNA
PanCK
CD3
CD127
CD161
CCR6
CD103
CD117
CD4
CD20
50 um
Merge
CD127 PanCK
CD161 PanCK
CD3 CD4 PanCK
CD103 PanCK
CD117 PanCK
20 um
h
ILC1s
P = 0.029
Number of cells per area (mm2)
100
10
1
0.1
0.01
CD161+
CD161−
CD103+
CD161+
CD161−
CD103+
CD161+
CD161−
CD103+
Intra-epithelial
Sub-epithelial
Deeper tissue

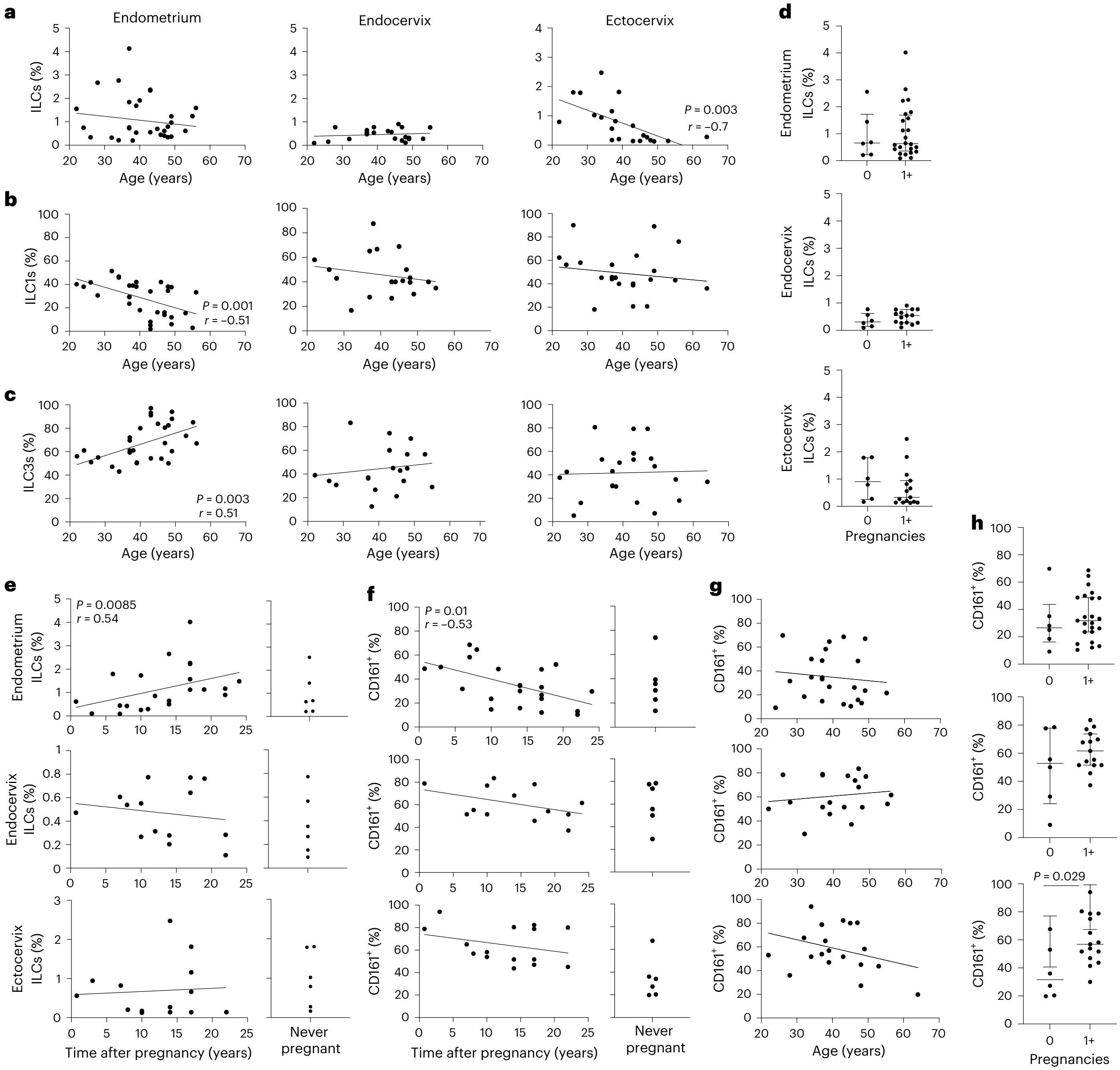

Fig. 5 | Age and prior pregnancies modify genital ILC subsets distribution. **a**, Spearman correlation of percentage of ILCs in mononuclear cells with age in the EM ($n = 31$), END ($n = 21$) and ECT ($n = 22$). **b**,**c**, Correlation of percentage of ILC1s (**b**) and ILC3s (**c**) in each tissue (EM, $n = 31$; END, $n = 20$; ECT, $n = 22$). **d**, Comparison of the percentage of ILCs in mononuclear cells between donors with and without prior pregnancies (EM, $n = 30$; END, $n = 21$; ETC, $n = 21$). **e**, Correlation of the percentage of ILCs in mononuclear cells in each tissue with time since last pregnancy. **f**, Correlation of percentage of CD161$^+$ ILCs in each tissue with time since last pregnancy (pregnant: EM, $n = 22$; END, $n = 13$; ECT, $n = 15$; never-pregnant: EM, $n = 6$; END, $n = 6$; ECT, $n = 6$). **g**, Correlation of percentage of CD161$^+$ ILCs in each tissue age (EM, $n = 23$; END, $n = 18$; ECT, $n = 15$). **h**, Comparison of CD161 expression between never-pregnant and previously pregnant patients (1+ pregnancies: EM, $n = 23$; END, $n = 15$; ECT, $n = 15$; no pregnancies: EM, $n = 6$; END, $n = 6$; ECT, $n = 6$). Each dot represents a different individual. Horizontal lines represent the median ± IQR. Spearman rank test for all correlations; non-parametric Mann–Whitney *U*-test for comparisons of two groups. All tests were two-sided.

lower numbers of endometrial ILCs than donors not recently pregnant (Fig. 5e). We observed no trend with donors who were never pregnant. Importantly, the effect of time after last pregnancy on ILC frequency was selective to the EM (Fig. 5e, top graph).

The CD161 ligand (LLT1) is highly expressed on trophoblastic cells in the placenta[33], so we investigated whether CD161 expression on ILCs was modulated by reproductive parameters. CD161 expression on endometrial ILCs negatively correlated with time after pregnancy, suggesting that as time passes from pregnancy, genital ILCs lose expression of CD161 (Fig. 5f). Interestingly, CD161 expression was not modified with age (Fig. 5g), suggesting that regulation of CD161 expression over time is associated with pregnancy only. To further explore this possibility, we compared CD161 expression in previously pregnant versus never-pregnant donors. We found that ILCs from previously pregnant donors in the ECT expressed higher levels of CD161 (Fig. 5h). These results show that genital ILCs are modified throughout the lifespan and with reproductive function in a compartmentalized manner in the FGT.

ILCs rapidly respond to HIV stimulation with transcriptional changes

To define the antiviral potential of genital ILCs, we performed CITE-seq on enriched genital mixed-cell suspensions before and after in vitro HIV stimulation for 30 min. This approach allowed us to determine the single-cell whole transcriptome profile along with surface protein expression concurrently immediately following HIV exposure and bypass fluorescence-activated cell-sorting, a prolonged process that can modify the phenotype of immune cells sensitive to their tissue microenvironment[34].

To identify ILCs, we selected immune cells (CD45$^+$; encoded by *PTPRC*) and filtered out cells positive for lineage markers based on surface protein expression (CD3, CD11b, CD11c, CD14, CD15, CD16 and CD19) (Fig. 6a). Within this population, we selected three clusters of interest that expressed *IL7R* for further analysis (clusters 3, 4 and 5) (Fig. 6b). We validated our selection by confirming expression of previously described ILC genes, such as *KLRB1*, *ZNF683* and *ITGAE*[15] (Fig. 6c), and exclusion of genes associated with NK cell transcriptional signatures, such as *EOMES, NCAM1* and *NCR1* (ref. 35), which were enriched in *IL7R*-low clusters (clusters 0, 1, 2, 6; Fig. 6d). This indicated that clusters 3, 4 and 5 are enriched for helper ILCs, and we proceeded to further characterize these ILC-enriched clusters.

We determined that clusters 3, 4 and 5 contained both ILC1 and ILC3 signatures (Fig. 6e–h). ILC1-associated genes such as *ITGA1*, *ZBTB16*, *IKZF3* and *TBX21* (refs. 14,15) were expressed across the uniform manifold approximation and project plot of genital ILCs (Fig. 6e). We also identified signature genes of intraepithelial ILC1s, such as *PRDM1* and *CD160* (Fig. 6f), previously described in the gut[15]. ILC3 signature genes were also detected throughout (*KIT*, *AHR*, *CCR6* and *LTB)*[14,15] (Fig. 6g). Additionally, genital ILCs expressed lymphoic tissue inducer (LTi)-associated genes such as *GPR183* and *NRP1* (refs. 36,37) (Fig. 6h).

To determine whether HIV exposure induces transcriptional changes in genital ILCs, we performed differential gene expression analysis between control and HIV-stimulated conditions in our ILC clusters. We identified genes upregulated and downregulated within 30 min following HIV exposure (Fig. 6i). Genital ILCs upregulated expression of *PRIM1* and *CXCL8*, which are important for cell proliferation and chemoattraction of myeloid cells, respectively. We also detected significant upregulation of *PLEK* (pleckstrin) (Fig. 6j), encoding a substrate for PKC in leukocytes, and an important intermediate in the secretion and activation pathways of proinflammatory cytokines like TNF and IL-1β[38]. Consistently, genital ILCs significantly upregulated *IL1B* and *TNF*, as well as *IL1R2*, encoding the IL-1 decoy receptor (Fig. 6j). Additionally, ILCs upregulated *BCL2A1*, encoding an anti-apoptotic protein, and *CD52*, encoding a surface glycoprotein involved in lymphocyte migration and activation. *ROMO1*, encoding a protein that increases reactive oxygen species (ROS), was also upregulated, suggesting ILCs respond to HIV through the increase in ROS (Fig. 6j).

We also identified genes downregulated with HIV stimulation (Fig. 6k). Genital ILCs downregulated expression of *CYGB* and *RHOBTB3*, both involved in limiting ROS production (Fig. 6k). Genes involved in preventing proliferation (*UBA7* and *CNOT3*) and cell death (*NINJ1)* were also downregulated. *DGAT1* expression, involved in the formation of lipid droplets responsible for creating an immunosuppressive environment, was also downregulated (Fig. 6k).

To further understand the overall genital ILC response to HIV, we performed Gene Ontology analysis of the statistically significant genes ($P \leq 0.05$) upregulated after stimulation and expressed in at least 10% of cells. Analysis of the upregulated genes, such as *IL7R*, *TNF*, *NLRP3, CD226* and *SLC11A1*, contributed to a term associated with regulation of the adaptive immune response through somatic recombination of immune receptors. We detected many pathways associated with innate immune processes. Genes like *NCKAP1L*, *IL1B*, *CXCL8*, *PDE4B* and *CSF3R* contributed to biological processes related to neutrophil chemotaxis (Fig. 6l). *HCK*, *IL1B*, *PDE4B*, *TNF* and *TICAM1* were involved in the term cellular response to lipopolysaccharide, suggesting potential activation of TLR4 by HIV[39]. We also detected terms associated with cell surface signaling, indicating that ILCs are undergoing an immediate response to the virus. Additionally, multiple pathways associated with ROS production were upregulated in response to HIV (Fig. 6l).

Overall, in response to HIV stimulation, genital ILCs triggered transcriptional signatures involved in inflammatory responses (cytokines and ROS), innate immune responses and cell proliferation.

ILCs respond to HIV through cytokine secretion and surface receptor modulation

Given that our data demonstrate that ILCs transcriptionally respond to HIV, we wanted to characterize the interactions between HIV and ILCs and the elicited responses at the protein level. First, we investigated HIV receptors. ILCs are not considered HIV-target cells, and whether they express HIV receptors is controversial[23,40]. Our flow cytometry analysis (Fig. 2c) demonstrated the presence of CD4$^+$ ILCs in the FGT. Therefore, we further investigated HIV receptor expression in genital ILCs in a larger cohort. ILCs expressed CD4 at low levels compared to CD4$^+$ T cells from the same tissue (Fig. 7a). CD4 expression was enriched on ILCs from the END and ECT compared to the EM (Fig. 7a,b) and was preferentially expressed on ILC1s (Fig. 7c). CD4$^+$ ILC1s were primarily CD161 low or negative (Fig. 7d). To verify our flow cytometry results with untouched cells, we investigated CD4 expression through ChipCytometry and identified CD4$^+$ ILC1s in the ECT (Fig. 7e). Evaluation of classical co-receptors showed that CCR5 was expressed by a portion of ILCs, with no tissue differences, but enriched on ILC1s (Extended Data Fig. 5a). By contrast, CXCR4 was broadly expressed in all ILCs and enriched in the ECT compared to the EM (Extended Data Fig. 5b). CD4/CCR5 co-expression is critical for mucosal HIV acquisition[41]. We detected a small percentage of ILCs co-expressing both receptors, primarily in END and ECT (Fig. 7f), suggesting potential viral entry through classical HIV receptors in a small subset of genital ILCs.

Next, we investigated initial ILC responses to HIV challenge (30 min) at the protein level. This time was chosen to reveal immediate ILC responses to HIV before viral infection or replication and determine whether genital ILCs can use their pre-formed cytokines as a first-line defense in antiviral responses.

After HIV challenge, we detected a reduction in intracellular IFNγ content together with increased degranulation (CD107a expression) in ILC1s (Fig. 7g). Interestingly, these changes were specific to CD161$^-$ ILC1s, the subset with high intracellular cytokine content at homeostasis (Fig. 3b), but we detected no response in CD161$^+$ ILC1s (Fig. 7g). IFNγ intracellular expression in CD161$^-$ ILC1s following HIV stimulation decreased by 83.15% relative to control (Extended Data Fig. 5c).

Fig. 6 | ILCs rapidly respond to HIV stimulation with transcriptional changes. **a**, Representative uniform manifold approximation and projection (UMAP) visualization of lineage-negative genital cells. **b**, UMAP plot of *IL7R* expression in lineage-negative genital cells from the EM, END and ECT. **c**,**d**, Gene expression of common human ILC (**c**) and NK-cell-associated genes (**d**). **e**–**h**, Gene expression for ILC1 (**e**), intraepithelial ILC1 (**f**), ILC3 (**g**) and LTI-like cells (**h**). **i**, Volcano plot of differentially expressed genes between control and HIV. Paired comparisons were done with the Wilcoxon non-parametric test (two-sided). Red indicates $P \leq 0.05$. **j**,**k**, Transcripts significantly upregulated (**j**) and downregulated (**k**) in response to HIV in genital ILCs. Red denotes HIV-stimulated; blue represents control. All have adjusted $P \leq 0.05$. **l**, Gene Ontology terms from upregulated genes ($P \leq 0.05$) with HIV stimulation. Fisher's exact test with false discovery rate (FDR) correction. FDR is shown by color; bubble size is the number of genes. $n = 3$ tissues (EM, END, ECT).

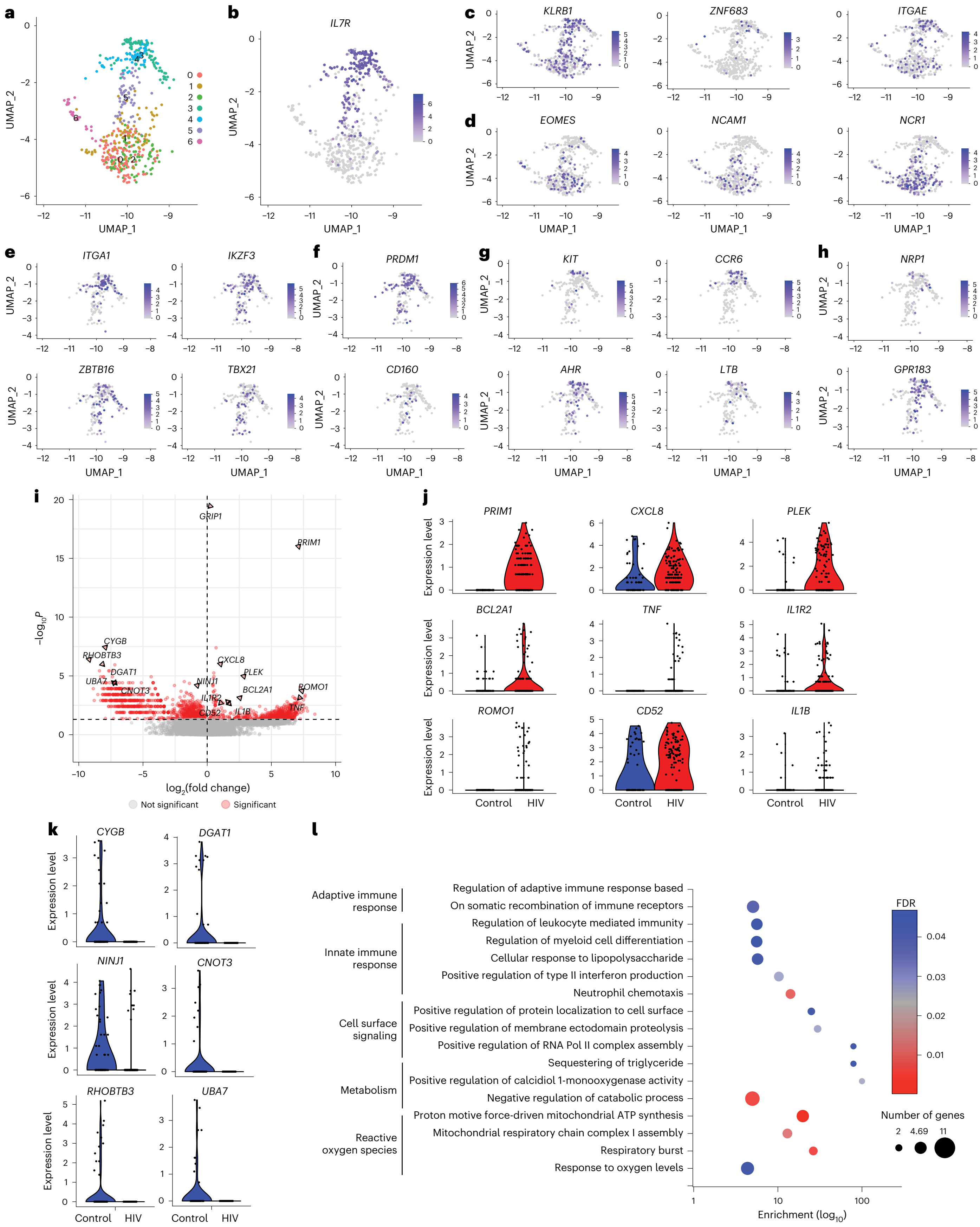
a
UMAP_2
UMAP_1
0
1
2
3
4
5
6
b
IL7R
c
KLRB1
ZNF683
ITGAE
d
EOMES
NCAM1
NCR1
e
ITGA1
IKZF3
ZBTB16
TBX21
f
PRDM1
CD160
g
KIT
CCR6
AHR
LTB
h
NRP1
GPR183
i
$-\log_{10}P$
$\log_2$(fold change)
GRIP1
PRIM1
CYGB
RHOBTB3
DGAT1
UBA7
CNOT3
NINJ1
CXCL8
PLEK
BCL2A1
ROMO1
IL1R2
CD52
IL1B
TNF
Not significant
Significant
j
Expression level
PRIM1
CXCL8
PLEK
BCL2A1
TNF
IL1R2
ROMO1
CD52
IL1B
Control
HIV
k
CYGB
DGAT1
NINJ1
CNOT3
RHOBTB3
UBA7
Control
HIV
l
Adaptive immune response
Innate immune response
Cell surface signaling
Metabolism
Reactive oxygen species
Regulation of adaptive immune response based
On somatic recombination of immune receptors
Regulation of leukocyte mediated immunity
Regulation of myeloid cell differentiation
Cellular response to lipopolysaccharide
Positive regulation of type II interferon production
Neutrophil chemotaxis
Positive regulation of protein localization to cell surface
Positive regulation of membrane ectodomain proteolysis
Positive regulation of RNA Pol II complex assembly
Sequestering of triglyceride
Positive regulation of calcidiol 1-monooxygenase activity
Negative regulation of catabolic process
Proton motive force-driven mitochondrial ATP synthesis
Mitochondrial respiratory chain complex I assembly
Respiratory burst
Response to oxygen levels
FDR
0.04
0.03
0.02
0.01
Number of genes
2
4.69
11
1
10
100
Enrichment ($\log_{10}$)

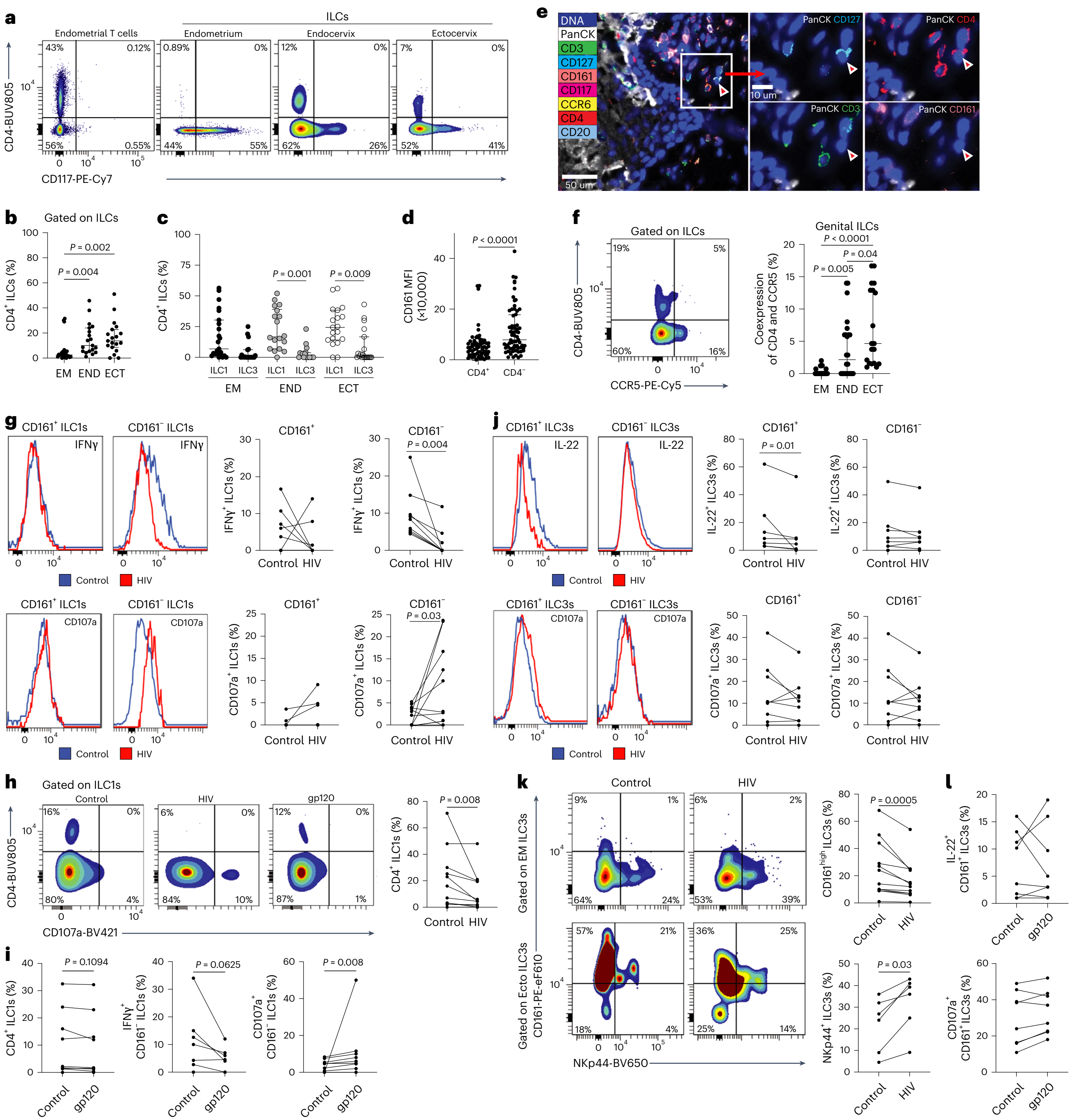

Fig. 7 | ILC subsets respond to HIV through cytokine secretion and surface receptor alterations. **a**, Representative contour plot of CD4 expression in genital T cells, EM, END and ECT ILCs. **b**, Percentage of ILCs expressing CD4 for each tissue type across all patients ($n = 60$ tissues: EM, $n = 24$; END, $n = 19$; ECT, $n = 19$). **c**, Percentage of CD4$^+$ ILC1s and ILC3s in each tissue ($n = 60$ tissues: EM, $n = 24$; END, $n = 18$; ECT, $n = 19$). **d**, Comparison of CD161 MFI between CD4$^+$ and CD4$^-$ ILCs ($n = 60$ tissues). **e**, Representative image of a CD4$^+$ ILC1 in the ECT. **f**, Representative contour plot of CD4 and CCR5 co-expression on ILCs (left) and quantification (right) (EM, $n = 24$; END, $n = 24$; ECT, $n = 19$). **g**, Histogram of IFNγ (top) and CD107a (bottom) expression in CD161$^+$ and CD161$^-$ ILC1s. Quantification of intracellular IFNγ and CD107a in control and HIV-stimulated ILC1s ($n = 9$). The connecting line represents one patient. **h**, Contour plot showing CD4 and CD107a expression in control ILC1s and stimulated with HIV and gp120. Quantification of CD4$^+$ ILC1s with and without HIV stimulation (right) ($n = 10$ tissues). **i**, Percentage of CD161$^-$ ILC1s that were CD4$^+$ (left), IFNγ$^+$ (middle) and CD107a$^+$ before and after gp120 stimulation ($n = 9$ tissues) **j**, Histogram of IL-22 (top) and CD107a (bottom) expression in CD161$^+$ and CD161$^-$ ILC3s. Quantification of intracellular IL-22 and CD107a in control and HIV-stimulated ILC3s (right). The connecting line represents one patient ($n = 9$). **k**, Contour plot representing CD161 and NKp44 expression on endometrial (top left) and ectocervical (bottom left) ILC3s stimulated with and without HIV. Percentage of CD161^{hi} (top right) ($n = 12$ tissues) and NKp44$^+$ ($n = 6$ tissues) (bottom right) ILC3s with HIV stimulation. **l**, Percentage of IL-22$^+$ (top) and CD107a$^+$ (bottom) CD161$^+$ ILC3s with and without gp120 stimulation ($n = 8$ tissues). Each dot represents a biological replicate. Horizontal lines represent the median ± IQR. Statistical analysis was performed using the non-parametric Kruskal–Wallis test (two-sided) with Dunn's post hoc test correction for multiple comparisons. Paired comparisons were done with the Wilcoxon non-parametric test (two-sided).

Additionally, granularity of CD161$^-$ ILC1s, but not in CD161$^+$ ILC1s, significantly decreased (measuring side scatter area; Extended Data Fig. 5d), suggesting granular release. Furthermore, genital ILC1s downregulated CD4 expression after HIV stimulation (Fig. 7h). As a control, genital T cells in the same sample did not downregulate CD4 upon 30 min of HIV stimulation (Extended Data Fig. 5e). To determine the mechanism for viral recognition, we performed stimulations with a CCR5-tropic gp120, the HIV glycoprotein that binds to CD4 and CCR5 (ref. 42). Following gp120 stimulation, we observed a significant increase in degranulation (CD107a) in genital CD161$^-$ ILC1s, but only a non-significant trend for decreased intracellular IFNγ content and no CD4 downregulation (Fig. 7i), suggesting that engagement of HIV receptors on ILC1s is only partially responsible for the observed effects.

Next, we evaluated ILC3 responses to HIV. Following HIV stimulation, CD161$^+$ ILC3s decreased intracellular IL-22 content, but not CD161$^-$ ILC3s (Fig. 7j). CD161$^+$ ILC3s exhibited about a 49.4% decrease in intracellular IL-22 following HIV stimulation relative to control (Extended Data Fig. 5c). In contrast to ILC1s, ILC3s did not increase CD107a expression upon HIV stimulation (Fig. 7j), but granularity (side scatter area) was reduced in CD161$^+$ ILC3s (Extended Data Fig. 5d), suggesting that IL-22 release is independent of CD107a. Additionally, we detected CD161 expression downregulation concurrently with NKp44 upregulation (Fig. 7k), suggesting a shift towards an activated phenotype[43]. Importantly, stimulation with gp120 did not elicit any IL-22 or CD107a responses on ILC3s (Fig. 7l), which lack CD4 expression (Fig. 7a). This lack of response suggests that recognition and response to HIV by ILC3s is not mediated through classical HIV receptors. Finally, we did not detect any changes in intracellular cytokines (IFNγ, IL-22) or degranulation (CD107a) in T cells or NK cells from the same samples within 30 min (Extended Data Fig. 5f), further emphasizing the significance of the prompt response of ILCs to HIV stimulation.

Discussion

We investigated the role of ILCs in human mucosal immunity within the FGT. We defined multiple genital ILC subpopulations and unraveled previously unknown anatomical compartmentalization of subsets, spatial distribution and function. Our study demonstrates constitutive production of cytokines and degranulation in a subset-specific and tissue-specific manner at homeostasis and demonstrates the ability of genital ILCs to respond to HIV challenge immediately upon exposure throughout the FGT. These findings uncover critical roles for human genital ILCs in controlling mucosal immunity at homeostasis and initiating antiviral responses following HIV exposure.

The genital mucosa is unique and different from other mucosal surfaces owing to the tight, cyclical hormonal regulation of immune cells to optimize conditions for reproduction[7]. Despite the indication from a limited number of studies that ILCs may be important for pregnancy, ILCs in the female genital mucosa (human and murine) remain vastly uncharacterized. In humans, helper ILCs have only been partly characterized in the EM or during pregnancy[21,22], but their role in mucosal protection during homeostasis and in response to infection throughout the FGT is completely unknown. Here we identified two genital ILC1 subpopulations (CD103$^+$ and CD103$^-$) and three ILC3 subpopulations (CCR6$^+$CD103$^+$, CCR6$^+$CD103$^-$ and CCR6$^-$) with tissue-dependent adaptations. Although CD103$^+$ ILC1s may represent intraepithelial ILC1s as described previously in the gut[44], genital ILC3s also express high levels of CD103 throughout. These data highlight the importance of studying each human mucosal site independently, as even within the FGT, ILCs possess tissue-specific phenotypes.

In our study, we uncovered that ILC1s and ILC3s constitutively produce IFNγ and IL-22, respectively, in the absence of stimulation. This production of cytokines seems to be enhanced in the FGT compared to other mucosal surfaces, as other studies reporting cytokine production by ILCs from lung[12], gut[13] and tonsil[18] required in vitro stimulation to detect cytokines. Given that IFNγ and IL-22 are important for antiviral responses and epithelial barrier maintenance, our findings suggest that genital ILCs are preloaded with cytokines critical to provide an antiviral tissue state before pathogen exposure and represent a rapid source of cytokines to initiate antiviral responses. We speculate that this phenotype may reflect a specialized homeostatic state shaped by the unique tissue environment and immunological demands of the FGT, which must balance tolerance for sperm and potential embryo implantation with defense against pathogens. This environment is subject to repeated microbial, inflammatory and hormonal fluctuations across the menstrual cycle, including cyclical changes in estrogen and progesterone that are known to modulate immunity and barrier integrity[5,7]. These factors may help maintain a partially activated ILC state that supports reproductive capacity while protecting tissue homeostasis. Future studies should examine how different hormonal, reproductive and inflammatory factors influence genital ILCs to determine the underlying mechanisms responsible for this 'primed' state in the FGT.

Moreover, we identified that CD161 expression was associated with high cytokine content in an opposite fashion between ILC1s and ILC3s. Although the role of CD161 in ILCs remains unclear, prior studies on NK cells indicate that engagement of CD161 with its ligand results in inhibited cytotoxicity and IFNγ secretion[45]. This would fit with our finding that CD161$^-$ ILC1s have increased production of IFNγ, but how CD161 expression influences ILC3 production of IL-22 deserves further investigation. Importantly, our findings provide a targetable molecule (CD161) to investigate the regulation of cytokine production by genital ILCs.

Another finding in our study is the identification of a unique LTi-like endometrial ILC3 subset (NKp44$^+$CCR6$^+$CD103$^-$) in adult human EM that constitutively degranulates at homeostasis and is located within endometrial lymphoid structures, interacting closely with T cells and B cells. Interestingly, contrary to our findings, prior studies in decidua reported that NKp44$^-$ ILC3s were more LTi-like than NKp44$^+$ ILC3s[21]. Unlike other mucosal surfaces, the female genital mucosa is not a classical mucosal inductive site, and the majority of T cells present are tissue-resident memory phenotype[28,29,46]. A previous porcine study has suggested that engagement of the natural cytotoxicity receptor NKp44 can lead to degranulation[47]. Location within lymphoid aggregates paired with constitutive degranulation selectively in the EM suggests that endometrial NKp44$^+$ ILC3s are degranulating within lymphoid aggregates after engagement of ligands on T cells and B cells, potentially to control their function. It remains to be determined what NKp44$^+$ ILC3s release through the CD107a-mediated degranulation pathway. Prior studies described lymphoid aggregate structures in the EM composed of B cells and memory T cells that cyclically develop during the menstrual cycle[48]. Whether sex hormones control NKp44$^+$ ILC3s to drive the formation and disassembly of lymphoid aggregates warrants further investigation. The presence of NKp44$^+$ ILC3s in these lymphoid aggregates, along with their degranulation capabilities, highlights their potential role in orchestrating immune responses outside of conventional cytokine secretion.

Interestingly, our analysis revealed changes in ILC diversity with age and prior pregnancies. These data support prior studies pointing to the involvement of ILCs in reproduction[21,22], but our study adds a level of complexity by uncovering dynamic changes in the human endometrial immune environment between pregnancies. Age and reproductive history represent a source of inter-individual variability that may influence the functional properties of genital ILCs under homeostasis and in response to pathogens, with potential consequences for innate mucosal protection and susceptibility to infections. Future studies need to determine whether sex hormones or specific tissue factors induced during pregnancy influence ILC plasticity.

Given that the initial immune responses triggered immediately after mucosal HIV exposure cannot be dissected in vivo, we investigated these responses using an in vitro model of mucosal HIV acquisition. Although ILCs have been studied in chronic HIV infection (in blood, gut and tonsils)[18,23,24], their potential involvement during initial mucosal exposure has not been investigated. Our study provides evidence that ILCs respond to HIV immediately after stimulation and represent a rapid source of effector cytokines in the FGT, a major portal of entry for HIV acquisition. Importantly, CD161 expression was a predictor of cytokine secretion by ILCs preloaded at homeostasis. IFNγ could have antiviral actions at multiple levels, including downregulation of CD4 to inhibit HIV entry into cells[49]. Paired with our imaging evidence that ILC1s are tightly associated with T cells in the genital mucosa, IFNγ production by ILC1s may protect T cells from infection. However, we also observed rapid CD4 downregulation on ILC1s following HIV stimulation, which could suggest viral internalization and susceptibility to infection. Whether ILC1s are targets for viral infection and replication remains controversial[23,40] and deserves further investigation, as they may represent previously unrecognized targets for HIV acquisition. Additionally, although ILC3s did not express classical HIV receptors, we detected antiviral responses with a rapid switch from a homeostatic CD161$^+$ phenotype to an activated NKp44$^+$ phenotype. Interestingly, in chronically simian immunodeficiency virus-infected animals, NKp44$^+$ ILCs negatively correlated with viral load, suggesting a protective effect of NCR$^+$ ILCs[50,51].

As our HIV stimulation assays were performed in the context of mixed-cell suspensions to mimic the mucosal environment, it remains undetermined whether genital ILCs directly recognize and respond to HIV or indirectly respond to inflammatory signals and secreted molecules from surrounding cells. Our attempts to purify genital ILCs resulted in low cell numbers, low viability, impure populations and artificial activation, as determined by increased CD107a expression and decreased intracellular cytokine content after the selection process. These technical issues represent a limitation of our study that prevented us from directly addressing this question and need to be overcome in future studies to obtain pure populations that accurately represent the functional state of ILCs in genital tissues. However, regardless of whether the response is direct or indirect, our study demonstrates that ILCs present in the genital mucosa are rapid responders following mucosal HIV exposure. Furthermore, although we speculate that ILC-mediated IFNγ and IL-22 responses could have a protective role, the biological role of this response for mucosal protection against HIV in vivo remains to be determined.

Overall, we demonstrate unique plasticity, location and functional roles for ILCs in the FGT at homeostasis, along with their ability to immediately respond to HIV challenge. These insights and our detailed phenotypic analysis pave the way for future research into the role of ILCs in human mucosal immunity and their potential involvement in HIV pathogenesis.

Online content

Any methods, additional references, Nature Portfolio reporting summaries, source data, extended data, supplementary information, acknowledgements, peer review information; details of author contributions and competing interests; and statements of data and code availability are available at https://doi.org/10.1038/s41590-025-02285-6.

References

1. Women and girls and HIV (2018). *UNAIDS* https://www.unaids.org/en/resources/documents/2018/women_girls_hiv (2018).
2. Boily, M. C. et al. Heterosexual risk of HIV-1 infection per sexual act: systematic review and meta-analysis of observational studies. *Lancet Infect. Dis.* **9**, 118–129 (2009).
3. Barr, F. D., Ochsenbauer, C., Wira, C. R. & Rodriguez-Garcia, M. Neutrophil extracellular traps prevent HIV infection in the female genital tract. *Mucosal Immunol.* **11**, 1420–1428 (2018).
4. Moreno de Lara, L. et al. Aging dysregulates neutrophil extracellular trap formation in response to HIV in blood and genital tissues. *Front. Immunol.* **14**, 1256182 (2023).
5. Rodriguez-Garcia, M., Connors, K. & Ghosh, M. HIV pathogenesis in the human female reproductive tract. *Curr. HIV/AIDS Rep.* **18**, 139–156 (2021).
6. Rodriguez-Garcia, M. et al. Dendritic cells from the human female reproductive tract rapidly capture and respond to HIV. *Mucosal Immunol.* **10**, 531–544 (2017).
7. Wira, C. R., Rodriguez-Garcia, M. & Patel, M. V. The role of sex hormones in immune protection of the female reproductive tract. *Nat. Rev. Immunol.* **15**, 217–230 (2015).
8. Parthasarathy, S. et al. Human genital dendritic cell heterogeneity confers differential rapid response to HIV-1 exposure. *Front. Immunol.* **15**, 1472656 (2024).
9. Vivier, E. et al. Innate lymphoid cells: 10 years on. *Cell* **174**, 1054–1066 (2018).
10. Panda, S. K. & Colonna, M. Innate lymphoid cells in mucosal immunity. *Front. Immunol.* **10**, 861 (2019).
11. Piersma, S. J. Tissue-specific features of innate lymphoid cells in antiviral defense. *Cell Mol. Immunol.* **21**, 1036–1050 (2024).
12. De Grove, K. C. et al. Characterization and quantification of innate lymphoid cell subsets in human lung. *PLoS ONE* **11**, e0145961 (2016).
13. Saez, A. et al. Innate lymphoid cells in intestinal homeostasis and inflammatory bowel disease. *Int. J. Mol. Sci.* **22**, 7618 (2021).
14. Mazzurana, L. et al. Tissue-specific transcriptional imprinting and heterogeneity in human innate lymphoid cells revealed by full-length single-cell RNA-sequencing. *Cell Res.* **31**, 554–568 (2021).
15. Jaeger, N. et al. Diversity of group 1 innate lymphoid cells in human tissues. *Nat. Immunol.* **25**, 1460–1473 (2024).
16. Yudanin, N. A. et al. Spatial and temporal mapping of human innate lymphoid cells reveals elements of tissue specificity. *Immunity* **50**, 505–519.e4 (2019).
17. Pascual-Reguant, A. et al. Multiplexed histology analyses for the phenotypic and spatial characterization of human innate lymphoid cells. *Nat. Commun.* **12**, 1737 (2021).
18. Singh, A. et al. Innate lymphoid cell activation and sustained depletion in blood and tissue of children infected with HIV from birth despite antiretroviral therapy. *Cell Rep.* **32**, 108153 (2020).
19. Cella, M. et al. Subsets of ILC3–ILC1-like cells generate a diversity spectrum of innate lymphoid cells in human mucosal tissues. *Nat. Immunol.* **20**, 980–991 (2019).
20. Bruggen, M. C. et al. In situ mapping of innate lymphoid cells in human skin: evidence for remarkable differences between normal and inflamed skin. *J. Invest. Dermatol.* **136**, 2396–2405 (2016).
21. Vacca, P. et al. Identification of diverse innate lymphoid cells in human decidua. *Mucosal Immunol.* **8**, 254–264 (2015).
22. Doisne, J. M. et al. Composition, development, and function of uterine innate lymphoid cells. *J. Immunol.* **195**, 3937–3945 (2015).
23. Kloverpris, H. N. et al. Innate lymphoid cells are depleted irreversibly during acute HIV-1 infection in the absence of viral suppression. *Immunity* **44**, 391–405 (2016).
24. Kramer, B. et al. Compartment-specific distribution of human intestinal innate lymphoid cells is altered in HIV patients under effective therapy. *PLoS Pathog.* **13**, e1006373 (2017).
25. Werner, A., Holmes, A., Moldovan, G. & Rodriguez-Garcia, M. Innate lymphoid cells in HIV pathogenesis and in the human female genital tract. *Curr. Opin. HIV AIDS* **20**, 117–123 (2025).
26. Parthasarathy, S. et al. Aging modifies endometrial dendritic cell function and unconventional double negative T cells in the human genital mucosa. *Immun. Ageing* **20**, 34 (2023).
27. Rodriguez-Garcia, M., Barr, F. D., Crist, S. G., Fahey, J. V. & Wira, C. R. Phenotype and susceptibility to HIV infection of CD4$^+$ Th17 cells in the human female reproductive tract. *Mucosal Immunol.* **7**, 1375–1385 (2014).

28. Rodriguez-Garcia, M., Fortier, J. M., Barr, F. D. & Wira, C. R. Aging impacts CD103$^+$ CD8$^+$ T cell presence and induction by dendritic cells in the genital tract. *Aging Cell* **17**, e12733 (2018).
29. Rodriguez-Garcia, M., Shen, Z., Fortier, J. M. & Wira, C. R. Differential cytotoxic function of resident and non-resident CD8$^+$ T cells in the human female reproductive tract before and after menopause. *Front. Immunol.* **11**, 1096 (2020).
30. Metcalfe, D. D. et al. Biomarkers of the involvement of mast cells, basophils and eosinophils in asthma and allergic diseases. *World Allergy Organ. J.* **9**, 7 (2016).
31. Ghosh, M. et al. CCL20/MIP3α is a novel anti-HIV-1 molecule of the human female reproductive tract. *Am. J. Reprod. Immunol.* **62**, 60–71 (2009).
32. Kang, J. et al. Type 3 innate lymphoid cells are associated with a successful intestinal transplant. *Am. J. Transpl.* **21**, 787–797 (2021).
33. Llibre, A. et al. Expression of lectin-like transcript-1 in human tissues. *F1000Res* **5**, 2929 (2016).
34. Llufrio, E. M., Wang, L., Naser, F. J. & Patti, G. J. Sorting cells alters their redox state and cellular metabolome. *Redox Biol.* **16**, 381–387 (2018).
35. Rebuffet, L. et al. High-dimensional single-cell analysis of human natural killer cell heterogeneity. *Nat. Immunol.* **25**, 1474–1488 (2024).
36. Chu, C. et al. Anti-microbial functions of group 3 innate lymphoid cells in gut-associated lymphoid tissues are regulated by G-protein-coupled receptor 183. *Cell Rep.* **23**, 3750–3758 (2018).
37. Shikhagaie, M. M. et al. Neuropilin-1 is expressed on lymphoid tissue residing LTi-like group 3 innate lymphoid cells and associated with ectopic lymphoid aggregates. *Cell Rep.* **18**, 1761–1773 (2017).
38. Ding, Y. et al. Phosphorylation of pleckstrin increases proinflammatory cytokine secretion by mononuclear phagocytes in diabetes mellitus. *J. Immunol.* **179**, 647–654 (2007).
39. Nazli, A. et al. HIV-1 gp120 induces TLR2- and TLR4-mediated innate immune activation in human female genital epithelium. *J. Immunol.* **191**, 4246–4258 (2013).
40. Zhao, J. et al. Infection and depletion of CD4$^+$ group-1 innate lymphoid cells by HIV-1 via type-I interferon pathway. *PLoS Pathog.* **14**, e1006819 (2018).
41. Saba, E. et al. HIV-1 sexual transmission: early events of HIV-1 infection of human cervico-vaginal tissue in an optimized ex vivo model. *Mucosal Immunol.* **3**, 280–290 (2010).
42. Yoon, V. et al. The GP120 molecule of HIV-1 and its interaction with T cells. *Curr. Med. Chem.* **17**, 741–749 (2010).
43. Vitale, M. et al. NKp44, a novel triggering surface molecule specifically expressed by activated natural killer cells, is involved in non-major histocompatibility complex-restricted tumor cell lysis. *J. Exp. Med.* **187**, 2065–2072 (1998).
44. Fuchs, A. et al. Intraepithelial type 1 innate lymphoid cells are a unique subset of IL-12- and IL-15-responsive IFN-γ-producing cells. *Immunity* **38**, 769–781 (2013).
45. Aldemir, H. et al. Cutting edge: lectin-like transcript 1 is a ligand for the CD161 receptor. *J. Immunol.* **175**, 7791–7795 (2005).
46. Shen, Z., Vom Steeg, L. G., Patel, M. V., Rodriguez-Garcia, M. & Wira, C. R. Impact of aging on the frequency, phenotype, and function of CD4$^+$ T cells in the human female reproductive tract. *Front. Immunol.* **15**, 1465124 (2024).
47. Mair, K. H. et al. The natural cytotoxicity receptor NKp44 (NCR2, CD336) is expressed on the majority of porcine NK cells ex vivo without stimulation. *Front. Immunol.* **13**, 767530 (2022).
48. Yeaman, G. R., Collins, J. E., Fanger, M. W., Wira, C. R. & Lydyard, P. M. CD8$^+$ T cells in human uterine endometrial lymphoid aggregates: evidence for accumulation of cells by trafficking. *Immunology* **102**, 434–440 (2001).
49. Kang, S., Brown, H. M. & Hwang, S. Direct antiviral mechanisms of interferon-gamma. *Immune Netw.* **18**, e33 (2018).
50. Rahman, M. A. et al. Differential effect of mucosal NKp44$^+$ innate lymphoid cells and Δγ cells on simian immunodeficiency virus infection outcome in rhesus macaques. *J. Immunol.* **203**, 2459–2471 (2019).
51. Rahman, M. A., Silva de Castro, I., Schifanella, L., Bissa, M. & Franchini, G. Vaccine induced mucosal and systemic memory NK/ILCs elicit decreased risk of SIV/SHIV acquisition. *Front. Immunol.* **15**, 1441793 (2024).

---

[1]Immunology Program, Tufts University School of Medicine, Boston, MA, USA. [2]Department of Biochemistry, Microbiology and Immunology, Wayne State University School of Medicine, Detroit, MI, USA. [3]C.S. Mott Center for Human Growth and Development, Wayne State University School of Medicine, Detroit, MI, USA. [4]Department of Immunology, Tufts University School of Medicine, Boston, MA, USA. [5]Department of Obstetrics and Gynecology at the Wayne State University School of Medicine, Detroit, MI, USA. [6]Department of Gynecology and Obstetrics, Tufts Medical Center, Boston, MA, USA. [7]Mass General Research Institute (MGRI), Division of Clinical Research, Massachusetts General Hospital, Boston, MA, USA. [8]These authors contributed equally: Laura Moreno de Lara, Aleah Holmes. ✉e-mail: Marta.rodriguez-garcia@wayne.edu

Methods

Study subjects

Studies were performed with Tufts University and Wayne State University Institutional Review Board approval. HIV-negative women undergoing hysterectomies for benign conditions at Tufts Medical Center or Detroit Medical Center gave written informed consent before surgery. Approval to use tissues was obtained from the Committee for the Protection of Human Subjects. Hysterectomy samples from three patients were obtained through the National Disease Research Interchange. Tissue samples distal from the sites of pathology and without pathological lesions were selected by pathologists. De-identified information about age, surgery indication, menstrual or menopausal status and reproductive history was collected. For patients obtained through the National Disease Research Interchange, only information about age was available. General characteristics of the patients are shown in Supplementary Table 1.

Tissue processing

Tissues obtained from hysterectomies included EM, END and ECT ($n = 110$ tissues from $n = 46$ patients) and were transferred to the laboratory immediately after surgery. Tissues were processed to obtain stromal mixed-cell suspensions with optimized protocols to preserve tissue intrinsic features of resident cells, as previously described[4,8]. In brief, enzymatic digestion was performed in a gentleMACS Dissociator (Miltenyi Biotec) using the Tumor Dissociation Kit, Human (Miltenyi Biotec) and 0.01% DNase (Worthington Biochemical). After digestion, the tissues were filtered through 100 µm, 70 µm and 30 µm filters (MACS SmartStrainers; Miltenyi Biotec) to separate epithelial cells from stromal cells. Cell suspensions then underwent red blood cell removal using human CD235a (Glycophorin A) MicroBeads (Miltenyi Biotec). Mixed-cell suspensions were used for high-dimensional spectral flow cytometry analysis.

Flow cytometry analysis

Mixed-cell suspensions were stained for surface markers with combinations of anti-human antibodies shown in Supplementary Table 2. Dead cells were excluded with the LIVE/DEAD Fixable Blue Dead Cell Stain Kit (Invitrogen). Following surface marker staining, intracellular staining was performed by washing, fixing and permeabilizing cells (20 min), following instructions provided in the Cytofix/Cytoperm Plus kit (BD Biosciences), and then staining for intracellular cytokines for 30 min. For samples that underwent transcription factor staining, after surface staining, cells were fixed and permeabilized using the eBioscience Foxp3/Transcription Factor Staining Kit and stained for transcription factors for 30 min. Analysis was performed on a spectral flow cytometer, the five-laser Aurora cytometer (Cytek Biosciences) or the three-laser Northern Lights (Cytek Biosciences). Data were analyzed with OMIQ software (www.omiq.ai). Expression of surface markers is shown as a percentage of positive cells and the mean fluorescence intensity. The fluorescence-minus-one strategy was used to establish appropriate gates. Unsupervised clustering analysis was performed using OMIQ software (www.omiq.ai). Data from three patients with matching FGT tissues (EM, END and ECT) were manually gated as shown in Fig. 1a to identify total ILCs (lineage-negative CD127$^+$). Then, opt-SNE[52], a dimensionality reduction method, was applied for visualization, followed by FlowSOM[53], a clustering algorithm to define genital ILC clusters based on marker expression.

Flow cytometry-based cytokine secretion assay

Secretion of IL-22 was determined using the flow-cytometry-based IL-22 Secretion Assay–Detection Kit (PE) (Miltenyi). The kit was used according to the manufacturer's instructions with modifications. Mixed-cell suspensions were generated and incubated on ice with the IL-22 catch reagent. After 5 min, the CD45 Spark NIR 685 antibody was added to the mixed-cell suspension, and cells were diluted in warm media as recommended. Cells were then stimulated with the Cell Activation Cocktail without Brefeldin A (a pre-mixed cocktail with PMA and ionomycin) (BioLegend) according to the manufacturer's instructions. CD107a antibody was added, and the cells were incubated for 1 h at 37 °C with slow rotation as recommended. After 1 h, cells were washed according to the manufacturer's instructions and incubated with the IL-22 detection antibody for 10 min as recommended. After 10 min, cells were labeled with the LIVE/DEAD Fixable Blue Dead Cell Stain Kit (Invitrogen) and incubated with antibodies for cell surface markers to detect ILCs as detailed in the 'Flow cytometry analysis' section.

ChipCytometry

The CellScape Precise Spatial Multiplexing platform was used for automated tissue staining and imaging (Canopy Biosciences, A Bruker Company). Tissues were fresh-frozen in OCT and sectioned before staining. In brief, tissue sections were loaded into CellScape Chips following the manufacturer's instructions. Tissues were stained with two to three fluorescently labeled antibodies at a time, followed by high-dynamic-range image acquisition of each fluorophore at a resolution of 182 nm per pixel. Fluorescent signal from all fluorophores was quenched through filtered photobleaching. Tissues were then washed with wash buffer and subjected to additional rounds of staining, imaging and photobleaching until all markers were completed. The antibodies used for staining are shown in Supplementary Table 3. Quantification of the ILC3 subset location was done by selecting regions of interest in which ILC3s were present, and either contained lymphoid aggregates or did not. For ILC1 subset location quantification, regions of interest were categorized as intraepithelial, subepithelial or deeper tissue, and the presence of different ILC1 subsets was compared between these regions. The number of cells per area was counted. Areas with no detected ILCs were assigned an arbitrary value of 0.1 (instead of 0) to allow representation on a log scale.

HIV viral growth

HIV-1-BaL (R5) isolates were acquired from the AIDS Research and Reference Reagent Program at the Division of AIDS, National Institute of Allergy and Infectious Diseases, National Institutes of Health, with contributions from S. Gartner, M. Popovic and R. Gallo[54], and were propagated in activated peripheral blood mononuclear cells as previously described[55].

HIV and gp120 stimulation

For in vitro HIV-stimulation experiments, mixed-cell suspensions were stimulated with HIV-1 BaL for 30 min at a multiplicity of infection of 0.5, after which residual virus was washed away. After washing, cells were stained for surface markers as indicated, followed by fixation and permeabilization (as described in the 'Flow cytometry analysis' section) and intracellular cytokine staining for 30 min. Data were acquired with the five-laser Aurora (Cytek Biosciences) or the three-laser Northern Lights (Cytek Biosciences). Stimulation with Recombinant BaL gp120 (National Institutes of Health HIV Reagent Program, cat. no. 4961) at 1 µg ml^{-1} was performed using the same methods as described above.

Sample preparation for multi-omic single-cell RNA sequencing with HIV stimulation

Single-cell transcriptome and surface antibody sequencing was performed using the BD Rhapsody platform. Mixed single-cell suspensions from hysterectomy samples obtained from three genital tissues (EM, END and ECT) were enriched for innate immune cells by magnetic bead removal of CD3$^+$, CD19$^+$, CD235a$^+$ red blood cells and fibroblasts as previously described[8]. Cells were incubated with HIV-BaL (multiplicity of infection, 0.5) in XVIVO-15 or media alone for 30 min. Cells were washed to remove free virus and then incubated with oligo-conjugated antibodies (Supplementary Table 4) and barcoded sample tags. Cells were then washed twice in MACS buffer to remove unbound antibodies and sample tags. Cells were counted and loaded onto separate

BD Rhapsody cartridges according to condition (HIV-stimulated or unstimulated controls). Next, polyA tail capture beads with unique molecular identifier barcodes were added to the microwells, followed by a lysis step to extract cellular RNA. Sequencing libraries were then created according to the manufacturer's instructions.

Single-cell CITE-seq analysis

FASTQ files with unaligned reads were produced using the NovaSeq6000 instrument. Gene counts were obtained by aligning and annotating the reads to the human genome. Downstream analyses were accomplished using the Seurat R software package (v.5.1; http://satijalab.org/seurat). After filtering out cells with a high mitochondrial content and low number of features, we performed scaling and normalization using the SCTransform algorithm. Principal component analysis was used to reduce the dimensionality of the data. Uniform manifold approximation and projection was used for visualization. To identify genital ILCs, we filtered out cells with elevated expression of CD3, CD19, CD11b, CD11c, CD16, CD14 and CD15 surface proteins. Next, we identified ILC-enriched cell clusters through *IL7R* expression. Differentially expressed genes were identified from control and HIV-stimulated cells using the 'FindMarkers' function, considering genes that were found in at least 10% of the cells for at least one condition. Gene Ontology biological processes were produced with the Gene Ontology resource (https://geneontology.org) using a gene list of upregulated genes ($P \leq 0.05$) with HIV stimulation, and pathways with a false discovery rate of ≤0.05 were chosen for visualization.

Statistics

Data analysis was performed using the GraphPad Prism 9.0 software. Comparison of two groups was performed with the non-parametric Mann–Whitney *U*-test or Wilcoxon paired test. Comparison of three or more groups was performed by applying the non-parametric Kruskal–Wallis test followed by Dunn's post hoc test to correct for multiple comparisons. A two-sided *P* value of <0.05 was considered statistically significant; exact *P* values are provided on the figures.

Reporting summary

Further information on research design is available in the Nature Portfolio Reporting Summary linked to this article.

Data availability

CITE-seq data have been deposited in the NCBI Gene Expression Omnibus repository under accession number GSE279775. Source data are provided with this paper.

Code availability

No custom code was generated in this study.

References

52. Belkina, A. C. et al. Automated optimized parameters for T-distributed stochastic neighbor embedding improve visualization and analysis of large datasets. *Nat. Commun.* **10**, 5415 (2019).
53. Van Gassen, S. et al. FlowSOM: using self-organizing maps for visualization and interpretation of cytometry data. *Cytometry A* **87**, 636–645 (2015).
54. Gartner, S. et al. The role of mononuclear phagocytes in HTLV-III/LAV infection. *Science* **233**, 215–219 (1986).
55. Rodriguez-Garcia, M. et al. Estradiol reduces susceptibility of CD4$^+$ T cells and macrophages to HIV-infection. *PLoS ONE* **8**, e62069 (2013).

Acknowledgements

We thank R. Wang for technical assistance. B. Malla, P. Josephs and A. Azimirad (Department of Gynecology and Obstetrics, Tufts Medical Center, Boston, MA) for their help with clinical coordination and patient recruitment and K. Murga (Biorepository at Tufts Medical Center) for tissue supply. This work was supported by the National Institutes of Health R01AG060801 (M.R.-G.), R21AI172065 (M.R.-G.), U01AG084766 (M.R.-G.) and Burroughs Wellcome Fund PATH award (1334236) (M.R.-G.). The David Thorley–Lawson Memorial Flow Cytometry Core Facility at Tufts University is supported by S10OD032201. The Microscopy, Imaging and Cytometry Resources Core at Wayne State is supported in part by National Institutes of Health Center grant P30 CA22453 to the Karmanos Cancer Institute and R50 CA251068-01 to K. Moin, Wayne State University.

Author contributions

M.R.-G. and A.W. conceptualized the study. A.W., J.F. and M.R.-G. conducted the formal analyses. M.R.-G., A.W., L.M., A.H., S.P., A.B., F.C.S., J.F. and G.M. developed the methodology. A.W., L.M., A.H., S.P., A.B., F.C.S., G.M. and M.R.-G. performed the investigation. A.V., V.I., J.S. and R.J. procured resources. A.W., M.R.-G. and J.F. visualized the study. M.R.-G., A.V. and V.I. were responsible for project administration. M.R.-G. supervised the research and acquired funding. A.W. and M.R.-G. wrote the original draft of the paper. M.R.-G., A.W., J.F., G.M., L.M., A.B., F.C.S., S.P. and A.H. contributed to editing; all authors reviewed and approved the final version.

Competing interests

The authors declare no competing interests.

Additional information

Extended data is available for this paper at https://doi.org/10.1038/s41590-025-02285-6.

Supplementary information The online version contains supplementary material available at https://doi.org/10.1038/s41590-025-02285-6.

Correspondence and requests for materials should be addressed to Marta Rodriguez-Garcia.

Peer review information *Nature Immunology* thanks Tamara Tilburgs and the other, anonymous, reviewers for their contribution to the peer review of this work. Peer reviewer reports are available. Primary Handling Editor: P. Jauregui, in collaboration with the *Nature Immunology* team.

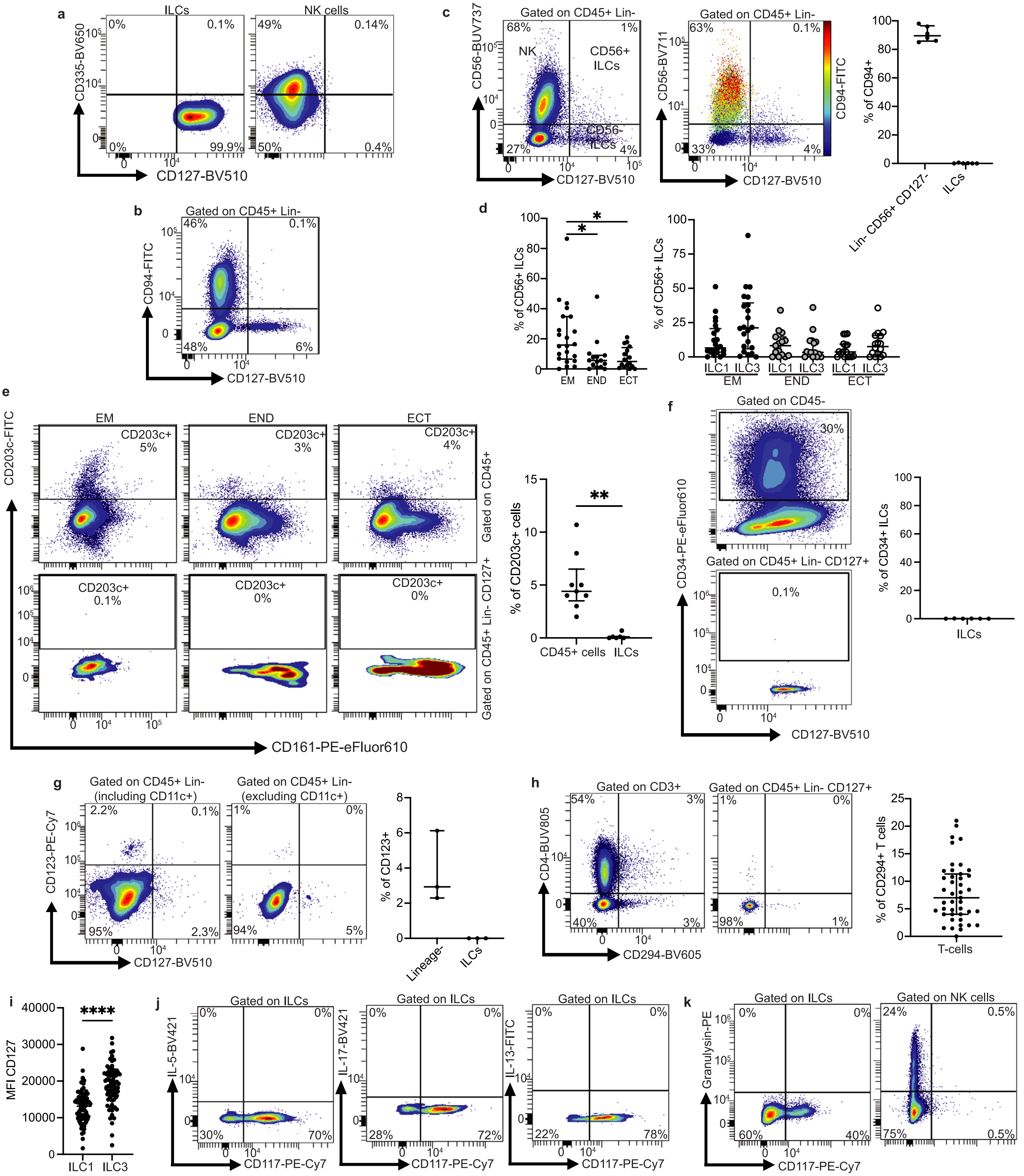

Extended Data Fig. 1 | See next page for caption.

Extended Data Fig. 1 | Genital helper ILCs are distinct from NK cells. (**a**) Contour plot of CD335 expression in ILCs (left) and NK cells (right). (**b**) Contour plot of CD94 expression vs CD127 expression in lineage negative cells. (**c**) Contour plot of CD56 expression in lineage negative cells (left) with CD94 expression overlayed in color (middle). Quantification of CD94+ Lineage negative CD56 + CD127- cells and ILCs (right) (n = 6 tissues). (**d**) Quantification of percent of ILCs expressing CD56 (left). Percent of CD56 + ILC1s and ILC3s across tissues (right). EM = 22, END = 15, ECT = 16. (**e**) Contour plots of CD203c expression in each tissue comparing total CD45+ (top) and genital ILCs (bottom). Quantification of CD203c expression in CD45+ and ILCs (right) (n = 9 tissues). (**f**) Contour plot of cells expressing CD34 in total CD45- (top) and genital ILCs (bottom) (n = 6). (**g**) Contour plots depicting percentage of CD123 expression in total CD45+ lineage- but including CD11c+ cells (left) and CD45+ lineage- CD11c- cells (middle). Quantification of CD123 expression (right) (n = 3 tissues) (**h**) Representative contour plot depicting CD294 and CD4 expression in CD3+ cells (left) and ILCs (right). Percent of CD294 + T-cells (CD3+) in different donors (n = 43 tissues). (**i**) CD127 MFI comparison between ILC1s and ILC3s in all tissues. (n = 56 tissues). (**j**) Representative contour plot of IL-5 (left), IL-17 (middle), and IL-13 (right) expression in genital ILCs. (**k**) Contour plot of Granulysin expression in genital ILCs (left) and NK cells (right) (n = 56 tissues). Each dot represents a biological replicate. Horizontal lines represent the median ± IQR. Statistical analysis was performed using the non-parametric Kruskal–Wallis test (two-sided) with Dunn's post-test correction for multiple comparisons. Paired comparisons were done with the Wilcoxon non-parametric test. *P < 0.05; **P < 0.01; ****P < 0.0001.

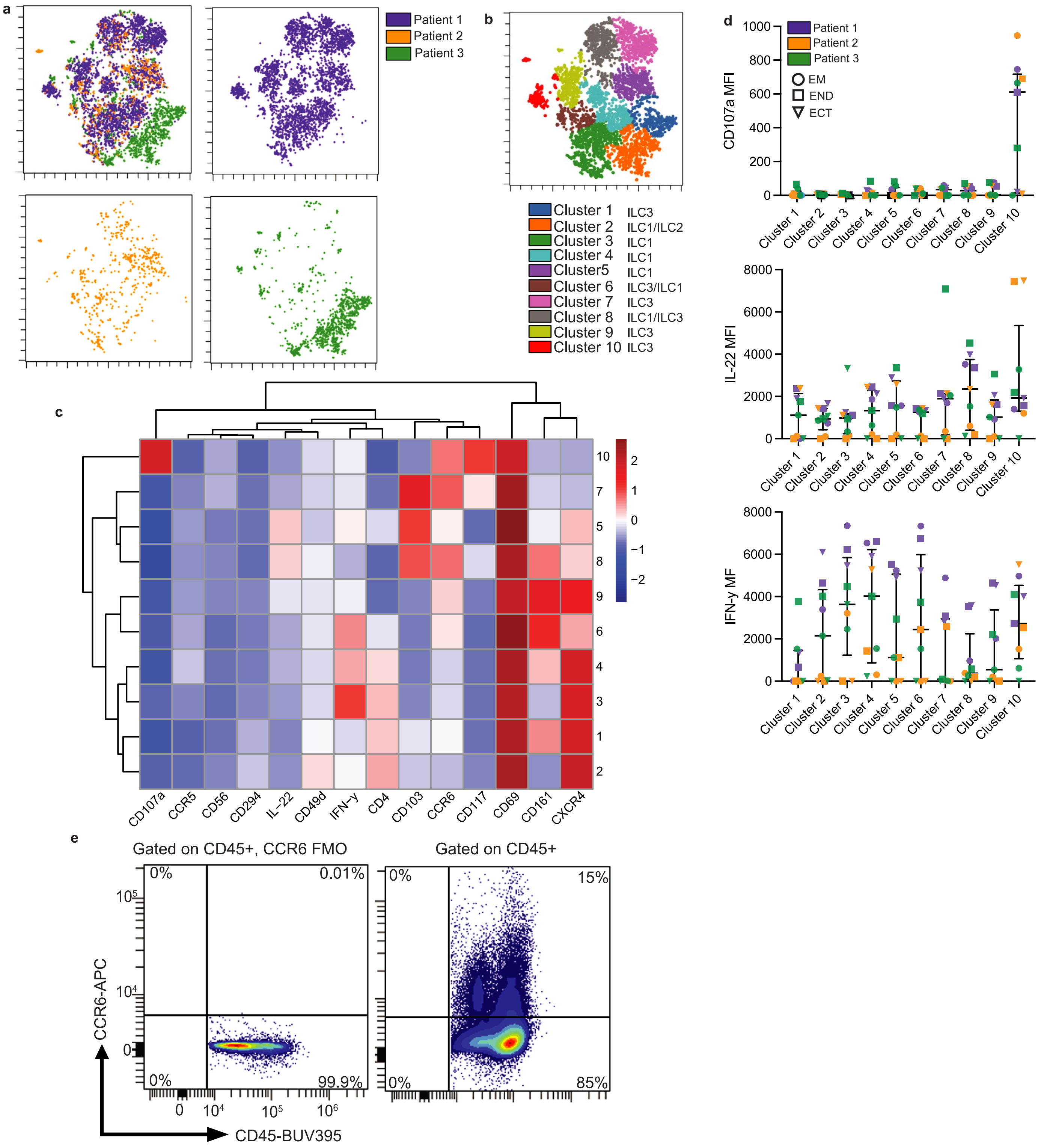

Extended Data Fig. 2 | Genital ILCs exhibit tissue- and patient-dependent protein expression differences. (**a**) opt-SNE plots on concatenated total ILCs from 3 matched patients' endometrium, endocervix, and ectocervix samples stratified by patient. (**b**) FlowSOM clustering analysis overlayed onto the opt-SNE plot with ten distinct clusters with matched ILC subset type. (**c**) Heatmap of the ten distinct clusters (rows) depicting the markers of interest with their relative expression values (red is high expression, blue is low). (**d**) MFI of CD107a (top), IL-22 (middle), and IFN-γ (bottom) by cluster. Shapes indicate tissue type, while color indicates patient. (**e**) Dot plot with an FMO (left) used to show detection of CCR6 in CD45+ genital cells (right).

https://doi.org/10.1038/s41590-025-02285-6

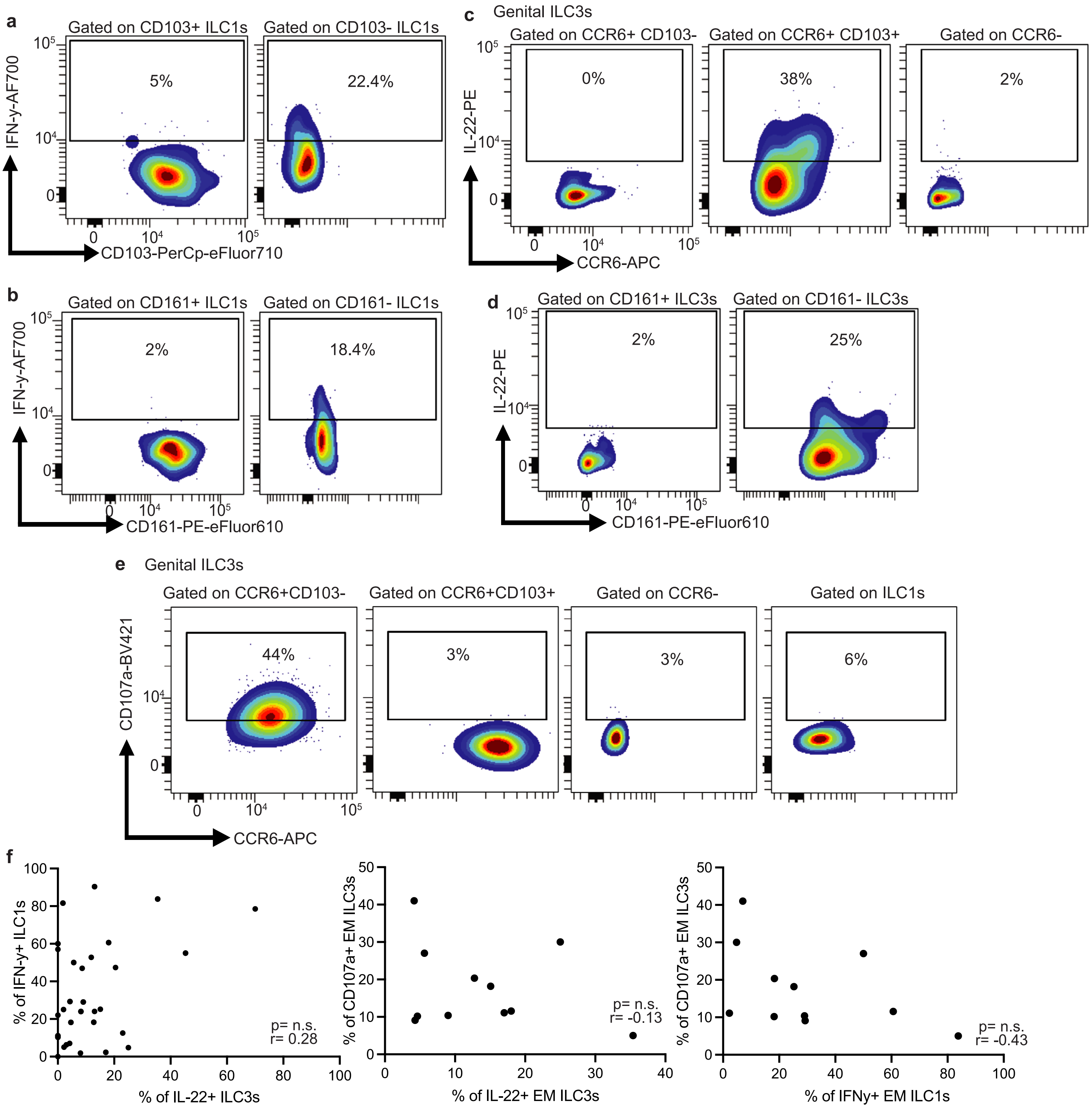

Extended Data Fig. 3 | Functionality of ILC subsets. (**a**) Contour plots depicting IFN-y expression in CD103+ (left) and CD103- (right) ILC1s. (**b**) Contour plots of IFN-y expression in CD161+ and CD161- ILC1s. (**c**) Contour plots of IL-22 expression in the three distinct ILC3 subsets, CCR6 + CD103-, CCR6 + CD103+, and CCR6-. (**d**) Contour plot of IL-22 expression in CD161+ and CD161- ILC3s. (**e**) Contour plot of CD107a expression in three ILC3 subsets and ILC1s. (**f**) Lack of correlation between percentage of IFN-y + ILC1s and IL-22 + ILC3s (top) (n = 32 tissues); endometrial CD107a + ILC3s and IL-22 + ILC3s (middle) (n = 11 tissues); and endometrial CD107a + ILC3s and IFN-y + ILC1s (bottom) (n = 11 tissues). Each dot represents one patient with both values. Spearman rank test (two-sided) for all correlations.

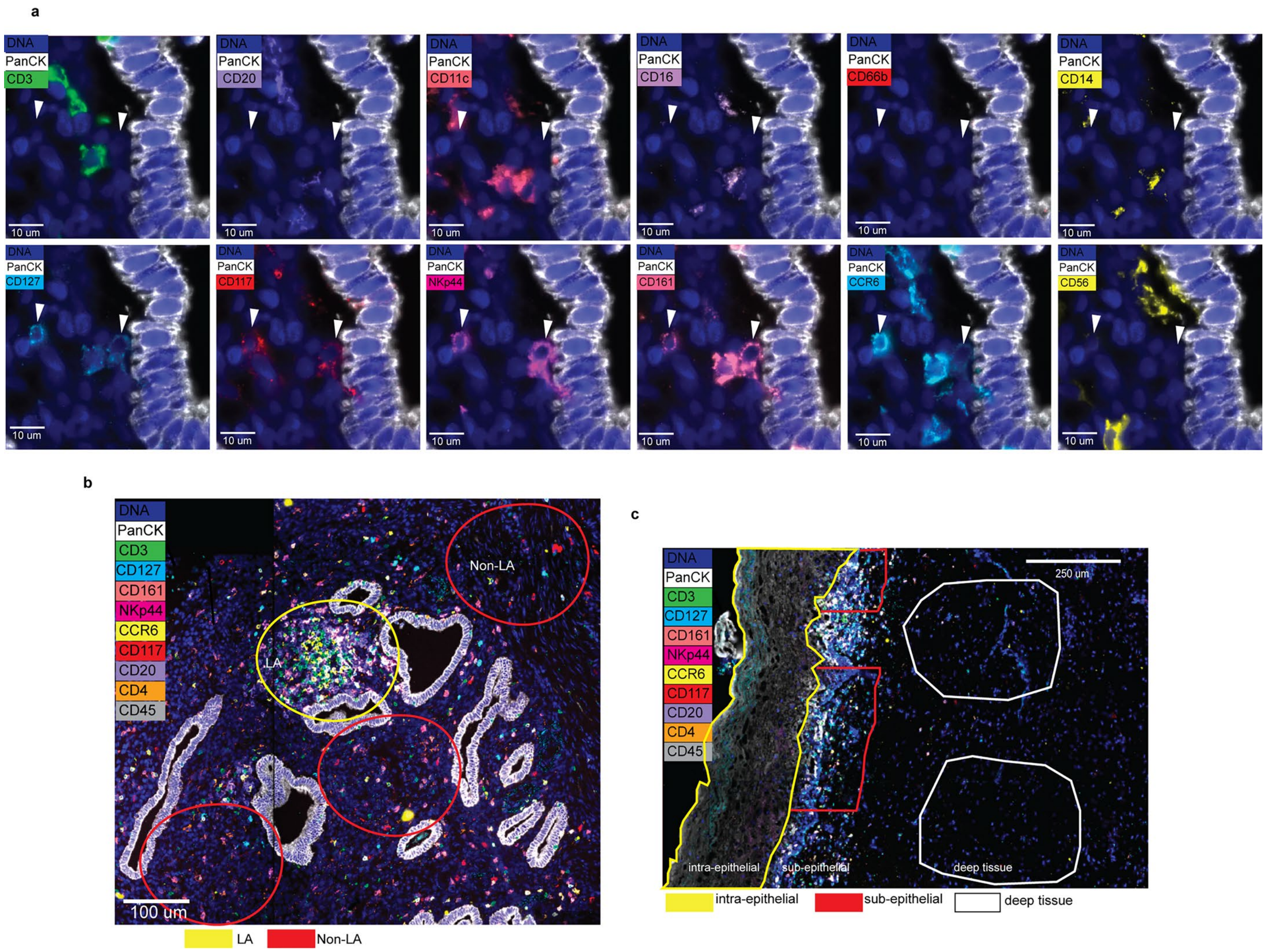

Extended Data Fig. 4 | Quantification of genital ILCs with ChipCytometry. (**a**) Representative fluorescent images depicting lineage markers and ILC markers to identify ILCs. (**b**) Representative example of selected regions of interest (ROI) for quantification of ILC3s in the endometrium according to location within lymphoid aggregates or outside lymphoid aggregates. Yellow depicts a representative ROI with a LA (lymphoid aggregate) and red depicts representative regions without lymphoid aggregates (non-LA). (**c**) Representative example of selected ROI in ectocervix for ILC1 quantification. Yellow depicts intraepithelial, red subepithelial, and white deeper tissue ROIs.

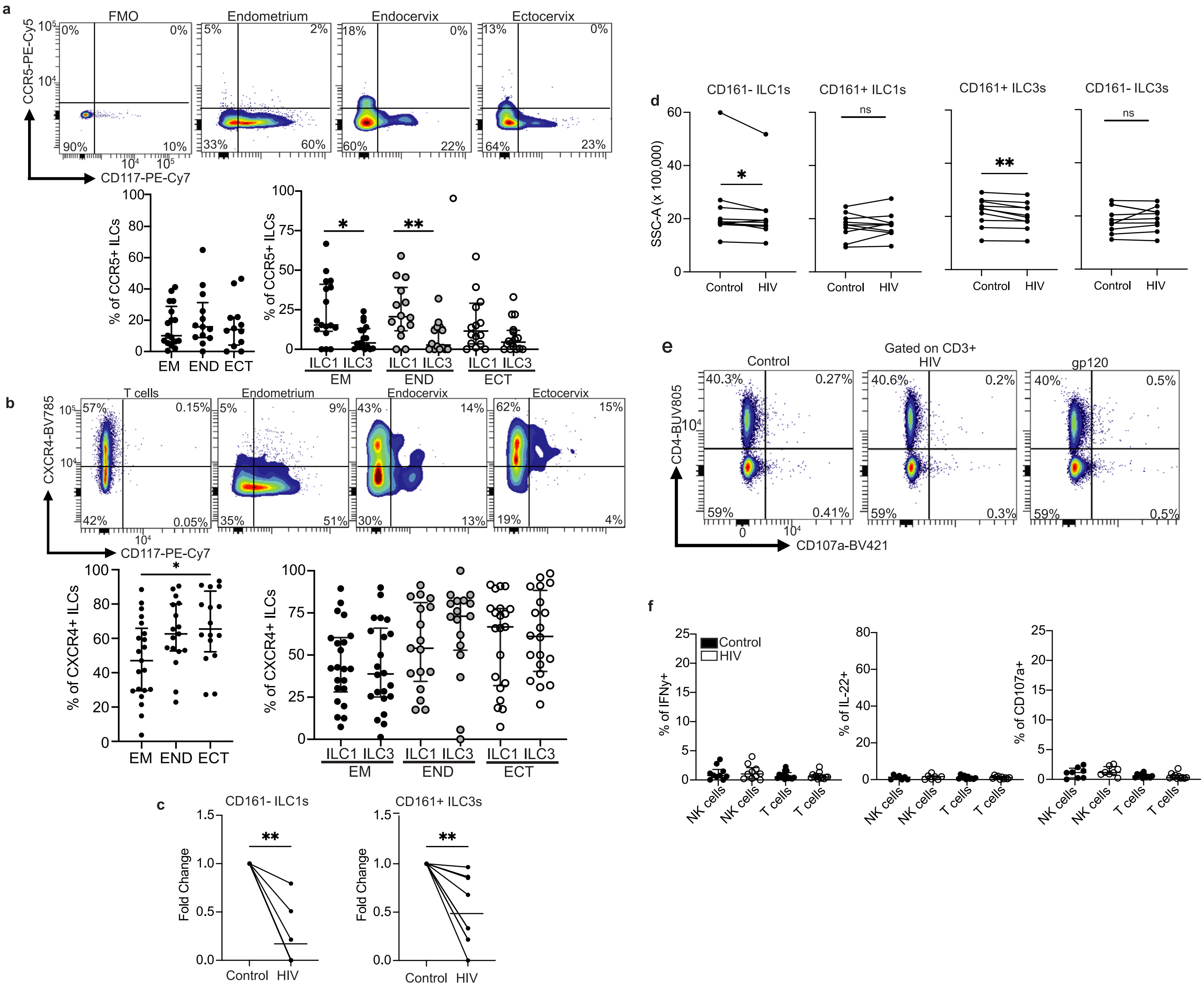

Extended Data Fig. 5 | Genital ILCs respond to HIV. (**a**) Contour plot of CCR5 expression in a fluorescent-minus-one (FMO), and genital ILCs (top). Percent of genital ILCs expressing CCR5 (bottom left), and percent of ILC1s and ILC3s expressing CCR5 (bottom right). EM (n = 17), END (n = 14), ECT (n = 15). (**b**) Contour plot of CXCR4 expression in T-cells and genital ILCs (top). Percent of genital ILCs expressing CXCR4 (bottom left), and percent of ILC1s and ILC3s expressing CXCR4 (bottom right). EM (n = 22), END (n = 17), ECT (n = 21). (**c**) Fold change in intracellular IFN-γ expression in CD161⁻ ILC1s (left) and IL-22 expression in CD161⁺ ILC3s (right) following HIV stimulation, normalized to their respective unstimulated controls (set to 1). Each line represents a matched individual tissue. Horizontal lines indicate the mean. Statistical significance was assessed using a one-sample Wilcoxon rank test. (**d**) Side scatter area comparison between control and HIV stimulated CD161+/- ILC1s and CD161+/- ILC3s. (n = 9 tissues) (**e**) CD4 and CD107a expression on CD3+ cells before and after HIV and gp120 stimulation. (**f**) Percent of IFN-y+ (left), IL-22+ (middle), and CD107a+ (right) NK cells (CD56 + CD127-) and T-cells (CD3+) with (white) and without (black) HIV stimulation. Wilcoxon test (two-sided). Each dot represents a patient (n = 9). Horizontal lines represent the median ± IQR. Statistical analysis was performed using the non-parametric Kruskal–Wallis test (two-sided) with Dunn's post-test correction for multiple comparisons. *P < 0.05; **P < 0.01.

nature portfolio

Corresponding author(s):	Marta Rodriguez-Garcia
Last updated by author(s):	Aug 14, 2025

Reporting Summary

Nature Portfolio wishes to improve the reproducibility of the work that we publish. This form provides structure for consistency and transparency in reporting. For further information on Nature Portfolio policies, see our Editorial Policies and the Editorial Policy Checklist.

Statistics

For all statistical analyses, confirm that the following items are present in the figure legend, table legend, main text, or Methods section.

n/a	Confirmed	
☐	☒	The exact sample size (*n*) for each experimental group/condition, given as a discrete number and unit of measurement
☐	☒	A statement on whether measurements were taken from distinct samples or whether the same sample was measured repeatedly
☐	☒	The statistical test(s) used AND whether they are one- or two-sided *Only common tests should be described solely by name; describe more complex techniques in the Methods section.*
☐	☒	A description of all covariates tested
☐	☒	A description of any assumptions or corrections, such as tests of normality and adjustment for multiple comparisons
☐	☒	A full description of the statistical parameters including central tendency (e.g. means) or other basic estimates (e.g. regression coefficient) AND variation (e.g. standard deviation) or associated estimates of uncertainty (e.g. confidence intervals)
☐	☒	For null hypothesis testing, the test statistic (e.g. *F*, *t*, *r*) with confidence intervals, effect sizes, degrees of freedom and *P* value noted *Give P values as exact values whenever suitable.*
☒	☐	For Bayesian analysis, information on the choice of priors and Markov chain Monte Carlo settings
☒	☐	For hierarchical and complex designs, identification of the appropriate level for tests and full reporting of outcomes
☐	☒	Estimates of effect sizes (e.g. Cohen's *d*, Pearson's *r*), indicating how they were calculated

Our web collection on statistics for biologists contains articles on many of the points above.

Software and code

Policy information about availability of computer code

Data collection	SpectroFlo Software version number is v3.3.0 was used for Flow cytometry data collection
Data analysis	GraphPad Prism 9.0 for statistical analysis Seurat R software package v5.1; Gene Ontology Resource (https://geneontology.org); OMIQ software (www.omiq.ai) for flow cytometry analysis QuPath v0.5.1 for bioimage analysis

For manuscripts utilizing custom algorithms or software that are central to the research but not yet described in published literature, software must be made available to editors and reviewers. We strongly encourage code deposition in a community repository (e.g. GitHub). See the Nature Portfolio guidelines for submitting code & software for further information.

Data

Policy information about availability of data

All manuscripts must include a data availability statement. This statement should provide the following information, where applicable:

- Accession codes, unique identifiers, or web links for publicly available datasets
- A description of any restrictions on data availability
- For clinical datasets or third party data, please ensure that the statement adheres to our policy

CITE-seq data have been deposited in the NCBI GEO repository under accession number GSE279775.

Research involving human participants, their data, or biological material

Policy information about studies with human participants or human data. See also policy information about sex, gender (identity/presentation), and sexual orientation and race, ethnicity and racism.

Reporting on sex and gender	This study is focused on the female reproductive tract, and therefore only includes female sex individuals.
Reporting on race, ethnicity, or other socially relevant groupings	Race and ethnicity was self-reported by the participants, but this information was not used in the analysis of the data.
Population characteristics	De-identified information about age, reason for hysterectomy, and prior obstetric history was collected and used for the analysis of the data. Only individuals undergoing hysterectomy for non-cancerous conditions were included. Reasons for surgery included conditions such as fibroids, prolapse, menorrhagia, dysmenorrhea or elective hysterectomy.
Recruitment	All HIV-negative individuals older than 18 y.o undergoing hysterectomy for non-cancerous conditions at TMC or DMC that signed the informed consent were included. Samples from 3 individuals were obtained through the National Disease Research Interchange (NDRI). No self-selection bias has been identified.
Ethics oversight	Tufts University Institutional Review Board and Wayne State University Institutional Review Board

Note that full information on the approval of the study protocol must also be provided in the manuscript.

Field-specific reporting

Please select the one below that is the best fit for your research. If you are not sure, read the appropriate sections before making your selection.

☒ Life sciences ☐ Behavioural & social sciences ☐ Ecological, evolutionary & environmental sciences

For a reference copy of the document with all sections, see nature.com/documents/nr-reporting-summary-flat.pdf

Life sciences study design

All studies must disclose on these points even when the disclosure is negative.

Sample size	A total of 110 tissues from 46 individuals were included. Samples size was determined based on tissue availability and immune cell distribution data in the female genital mucosa from our prior publications (Parthasarathy et al., 2024, PMC11543421; Moreno de Lara et al., 2023, PMC10684664; Parthasarathy et al., 2023, PMC10347869; Rodriguez-Garcia et al., 2020, PMC7287154)
Data exclusions	No data was excluded from the analyses
Replication	Experimental findings were repeated with multiple tissues for each experiment (biological replicates). The number of biological replicates is indicated in the figure legends. Experiments were reproducible. Flow flow cytometry experiments, a minimum of 4 biological replicates was used, but the majority of experiments include 10 or more biological replicates. For ChipCytometry we used 9 tissues from three donors. For CITE-seq experiments, three tissues were sample-tagged and pooled for sequencing.
Randomization	Allocation was random
Blinding	Blinding was not relevant to the study. Specimens were used as they became available for each set of experiments.

Reporting for specific materials, systems and methods

We require information from authors about some types of materials, experimental systems and methods used in many studies. Here, indicate whether each material, system or method listed is relevant to your study. If you are not sure if a list item applies to your research, read the appropriate section before selecting a response.

Materials & experimental systems

n/a	Involved in the study
☐	☒ Antibodies
☒	☐ Eukaryotic cell lines
☒	☐ Palaeontology and archaeology
☒	☐ Animals and other organisms
☒	☐ Clinical data
☒	☐ Dual use research of concern
☒	☐ Plants

Methods

n/a	Involved in the study
☐	☐ ChIP-seq
☐	☒ Flow cytometry
☐	☐ MRI-based neuroimaging

Antibodies

Antibodies used

All antibodies were used at a 1:100 dilution.
CD45 H130 BUV395 BD Biosciences 563792
CD56 NCAM16.2 BUV737 BD Biosciences 612767
CD4 SK3 BUV805 BD Biosciences 612888
IL-5 TRFK5 BV421 Biolegend 504311
IL-13 JES10-5A2 BV421 Biolegend 501915
IL-17 BL168 BV421 Biolegend 512321
T-bet 4B10 BV421 Biolegend 644815
CD107a H4A3 BV421 Biolegend 328625
IL-13 85BRD FITC Thermo Fisher 11-7136-41
IL-17 BL168 FITC Biolegend 512303
CD19 SJ25-C1 Pacific Blue Thermo Fisher MHCD1928
CD11b ICRF44 Pacific Blue Biolegend 301316
CD16 3G8 Pacific Blue Biolegend 302032
CD14 TuK4 Pacific Blue Thermo Fisher MHCD1428
CD127 A019D5 BV510 Biolegend 351331
CD294 BM16 BV605 Biolegend 350121
CD335 9E2 BV650 Biolegend 331927
CD336 p44-8 BV650 BD Biosciences 744302
CD49d SK11 BV711 Biolegend 304331
CXCR4 12G5 BV785 Biolegend 306529
CD3 UCHT1 AF532 Thermo Fisher 58-0038-42
CD3 SK7 APC Fire 810 Biolegend 344857
CD103 Ber-ACT8 PerCP-eF710 Thermo Fisher 46-1037-42
IL-22 2G12A41 PE Biolegend 366703
GATA-3 TWAJ PE Thermo Fisher 50-113-25
Granulysin DH2 PE Biolegend 348003
CD161 HP-3610 PE-eF610 Thermo Fisher 61-1619-42
CCR5 2D7/CCR5 PE-Cy5 BD Biosciences 556889
CD69 CH/4 PE-Cy5.5 Thermo Fisher MHCD6918
CD117 104D2 PE-Cy7 Biolegend 313211
CCR6 G034E3 APC Biolegend 353416
IFN-y 4S.B3 Alexa Fluor 700 Biolegend 502519
RORyt 1181A Alexa Fluor 700 Thermo Fisher IC9125N100
CD11c Bu15 APC-Cy7 Biolegend 337217
LIVE/DEAD LIVE/DEAD Blue Thermo Fisher L23105
panCK C-11 PE Novus NBP1-48348PE
CD127 A019D5 AF488 Biolegend 351313
CD161 HP-3G10 PE Biolegend 339903
Anti-AF488 - Quench Invitrogen A11094
CD56 5.1H11 PE BioLegend 981202
CD11c S-HCL-3 FITC BioLegend 371516
CD14 HCD14 PE Biolegend 325606
CD20 L26 AF488 Invitrogen 53020282
CD3 UCHT1 BUV395 BD 563546
CD4 RPA-T4 PerCP-Cy5.5 BioLegend 300530
CD16 DJ130C PE Invitrogen MA5-16647 (PIMA516647)
Anti-AF488 - Quench Invitrogen A11094
CD45 HI30 BUV395 BD 563792
C66b G10F5 PE Biolegend 305105
CD196 G034E3 PE Biolegend 353410
CD103 2E7 AF488 Biolegend 121407
CD117 104D2 PE Biolegend 313203
CD336 P44-8 PE Biolegend 325107
CD203c NP4D6 FITC Biolegend 324613
CD34 4H11 PE-ef610 Thermo Fisher 61-0349-42
CD94 DX22 FITC Biolegend 305504
CD123 6H6 PE-Cy7 Biolegend 306009

	CD45 2D1 Spark NIR 685 Thermo Fisher 50-207-8443 CD56 HCD56 BV711 Biolegend 318335
Validation	All antibodies used were directly conjugated and commercially available and quality-controlled by the companies (Specificity testing of 1-3 target cell types with either single- or multi-color analysis (including positive and negative cell types. Once specificity is confirmed, each new lot must perform with similar intensity to the in-date reference lot. Brightness (MFI) is evaluated from both positive and negative populations. Each lot product is validated by QC testing with a series of titration dilutions.) Antibody combinations were optimized and internal negative and positive controls were used. Unstained controls, Fluorescence minus one (FMO) controls, and reference controls (samples with only one antibody) were used to define specific staining and determine gating strategies. Antibodies were also validated comparing expression patterns between peripheral blood mononuclear cells and tissue cells (particularly for tissue-residency markers). Antibodies had also been validated in prior publications by us and others.

Plants

Seed stocks	*Report on the source of all seed stocks or other plant material used. If applicable, state the seed stock centre and catalogue number. If plant specimens were collected from the field, describe the collection location, date and sampling procedures.*
Novel plant genotypes	*Describe the methods by which all novel plant genotypes were produced. This includes those generated by transgenic approaches, gene editing, chemical/radiation-based mutagenesis and hybridization. For transgenic lines, describe the transformation method, the number of independent lines analyzed and the generation upon which experiments were performed. For gene-edited lines, describe the editor used, the endogenous sequence targeted for editing, the targeting guide RNA sequence (if applicable) and how the editor was applied.*
Authentication	*Describe any authentication procedures for each seed stock used or novel genotype generated. Describe any experiments used to assess the effect of a mutation and, where applicable, how potential secondary effects (e.g. second site T-DNA insertions, mosiacism, off-target gene editing) were examined.*

ChIP-seq

Data deposition

☐ Confirm that both raw and final processed data have been deposited in a public database such as GEO.

☐ Confirm that you have deposited or provided access to graph files (e.g. BED files) for the called peaks.

Data access links *May remain private before publication.*	*For "Initial submission" or "Revised version" documents, provide reviewer access links. For your "Final submission" document, provide a link to the deposited data.*
Files in database submission	*Provide a list of all files available in the database submission.*
Genome browser session (e.g. UCSC)	*Provide a link to an anonymized genome browser session for "Initial submission" and "Revised version" documents only, to enable peer review. Write "no longer applicable" for "Final submission" documents.*

Methodology

Replicates	*Describe the experimental replicates, specifying number, type and replicate agreement.*
Sequencing depth	*Describe the sequencing depth for each experiment, providing the total number of reads, uniquely mapped reads, length of reads and whether they were paired- or single-end.*
Antibodies	*Describe the antibodies used for the ChIP-seq experiments; as applicable, provide supplier name, catalog number, clone name, and lot number.*
Peak calling parameters	*Specify the command line program and parameters used for read mapping and peak calling, including the ChIP, control and index files used.*
Data quality	*Describe the methods used to ensure data quality in full detail, including how many peaks are at FDR 5% and above 5-fold enrichment.*
Software	*Describe the software used to collect and analyze the ChIP-seq data. For custom code that has been deposited into a community repository, provide accession details.*

Flow Cytometry

Plots

Confirm that:

☒ The axis labels state the marker and fluorochrome used (e.g. CD4-FITC).

☒ The axis scales are clearly visible. Include numbers along axes only for bottom left plot of group (a 'group' is an analysis of identical markers).

☒ All plots are contour plots with outliers or pseudocolor plots.

☒ A numerical value for number of cells or percentage (with statistics) is provided.

Methodology

Sample preparation	Tissues obtained from hysterectomies included endometrium EM), endocervix (END) and ectocervix (ECT) and were transferred to the laboratory immediately after surgery. Tissues were processed to obtain a stromal cell suspension as previously described6,78. Briefly, enzymatic digestion was performed in a gentleMACS™ Dissociator (Miltenyi Biotec) using Tumor Dissociation Kit, human (Miltenyi Biotec) and 0.01% DNAse (Worthington Biochemical, Lakewood, NJ). After digestion, the tissues were filtered through 100µm, 70µm, and 30µm filters (MACS® SmartStrainers; Miltenyi Biotec) to separate epithelial cells from stromal cells. Cell suspensions then underwent red blood cell removal using human CD235a (Glycophorin A) MicroBeads (Miltenyi Biotec). Mixed cell suspensions were used for flow cytometry analysis.
Instrument	Analysis was performed on a spectral flow cytometer, the 5-laser Aurora cytometer (Cytek Biosciences; Fremont, CA) or the 3-laser Northern Lights (Cytek Biosciences; Fremont, CA).
Software	Data was analyzed with OMIQ software (www.omiq.ai).
Cell population abundance	No flow cell sorting was performed for this study. Flow cytometry was performed using mixed cell suspensions enriched generated as described in sample preparation. Between half a million to one million cells were used per experiment.
Gating strategy	1) FSC-A and SS-A; 2) Singlets (FSC-A/FSC-H); 3) Live cells (Live/dead blue); 4) CD45+ (CD45/SSC-A); 5) Lineage negative cells (cells that lacked canonical lineage (Lin) markers [CD3, CD19, CD11b, CD14, CD16, CD66b, CD11c]; 6) CD127+ (ILCs are defined as CD45+, Lin-, CD127+), CD127 was determined with FMO strategy; 7) Determination of ILC subset (CD294/CD117); 8) Expression of additional markers within each ILC subset (CD103, CD69, CD161, CCR6.....). FMO strategy was used to determine subsets of ILCs.

☒ Tick this box to confirm that a figure exemplifying the gating strategy is provided in the Supplementary Information.

Magnetic resonance imaging

Experimental design

Design type	*Indicate task or resting state; event-related or block design.*
Design specifications	*Specify the number of blocks, trials or experimental units per session and/or subject, and specify the length of each trial or block (if trials are blocked) and interval between trials.*
Behavioral performance measures	*State number and/or type of variables recorded (e.g. correct button press, response time) and what statistics were used to establish that the subjects were performing the task as expected (e.g. mean, range, and/or standard deviation across subjects).*

Acquisition

Imaging type(s)	*Specify: functional, structural, diffusion, perfusion.*
Field strength	*Specify in Tesla*
Sequence & imaging parameters	*Specify the pulse sequence type (gradient echo, spin echo, etc.), imaging type (EPI, spiral, etc.), field of view, matrix size, slice thickness, orientation and TE/TR/flip angle.*
Area of acquisition	*State whether a whole brain scan was used OR define the area of acquisition, describing how the region was determined.*

Diffusion MRI ☐ Used ☐ Not used

Preprocessing

Preprocessing software	*Provide detail on software version and revision number and on specific parameters (model/functions, brain extraction, segmentation, smoothing kernel size, etc.).*

Normalization	*If data were normalized/standardized, describe the approach(es): specify linear or non-linear and define image types used for transformation OR indicate that data were not normalized and explain rationale for lack of normalization.*
Normalization template	*Describe the template used for normalization/transformation, specifying subject space or group standardized space (e.g. original Talairach, MNI305, ICBM152) OR indicate that the data were not normalized.*
Noise and artifact removal	*Describe your procedure(s) for artifact and structured noise removal, specifying motion parameters, tissue signals and physiological signals (heart rate, respiration).*
Volume censoring	*Define your software and/or method and criteria for volume censoring, and state the extent of such censoring.*

Statistical modeling & inference

Model type and settings	*Specify type (mass univariate, multivariate, RSA, predictive, etc.) and describe essential details of the model at the first and second levels (e.g. fixed, random or mixed effects; drift or auto-correlation).*
Effect(s) tested	*Define precise effect in terms of the task or stimulus conditions instead of psychological concepts and indicate whether ANOVA or factorial designs were used.*

Specify type of analysis: ☐ Whole brain ☐ ROI-based ☐ Both

Statistic type for inference (See Eklund et al. 2016)	*Specify voxel-wise or cluster-wise and report all relevant parameters for cluster-wise methods.*
Correction	*Describe the type of correction and how it is obtained for multiple comparisons (e.g. FWE, FDR, permutation or Monte Carlo).*

Models & analysis

n/a	Involved in the study
☐	☐ Functional and/or effective connectivity
☐	☐ Graph analysis
☐	☐ Multivariate modeling or predictive analysis

Functional and/or effective connectivity	*Report the measures of dependence used and the model details (e.g. Pearson correlation, partial correlation, mutual information).*
Graph analysis	*Report the dependent variable and connectivity measure, specifying weighted graph or binarized graph, subject- or group-level, and the global and/or node summaries used (e.g. clustering coefficient, efficiency, etc.).*
Multivariate modeling and predictive analysis	*Specify independent variables, features extraction and dimension reduction, model, training and evaluation metrics.*